Available online at www.sciencedirect.com
SCIENCE DIRECT
International Journal of Heat and Mass Transfer 49 (2006) 2058–2076
International Journal of HEAT and MASS TRANSFER
www.elsevier.com/locate/ijhmt

Effects of exit-condition, gravity, and surface-tension on stability and noise-sensitivity issues for steady condensing flows inside tubes and channels

L. Phan, X. Wang, A. Narain *

Department of Mechanical Engineering-Engineering Mechanics, Michigan Technological University, Houghton, MI 49931, United States

Received 23 May 2005; received in revised form 1 December 2005
Available online 28 February 2006

Abstract

The paper presents accurate numerical solutions of the full 2D governing equations for steady and unsteady laminar/laminar internal condensing flows of pure vapor (FC-72 and R-113) inside a vertical tube and a channel. The film condensation is on the inside wall of a tube or one of the walls of a channel (the lower wall in case of a downward sloping channel). Computations find that exit condition specifications are important and are able to characterize the flows' sensitivity or insensitivity to the exit condition (which, in turn, depends upon the flow downstream of the condenser). If well-defined natural steady/quasi-steady flows exist—as is shown to be the case for gravity dominated or strong shear dominated condensate flows that remain *parabolic* up to the exit location—the computations are able to predict both the natural exit condition and any point of transition (from stable to unstable or smooth to wavy behavior) that may exist within this zone. Results on the role of surface tension and sensitivity to ever-present minuscule noise of the condensing surface are also reported.

Keywords: Film condensation; Phase-change; Two-phase flows; Interfacial stability; Interfacial waves

1. Introduction

Sufficiently accurate numerical solutions of the full governing equations are presented for steady and unsteady laminar/laminar film condensation flows. The in-tube geometry (see Fig. 1a) is considered here while some new and improved results for the horizontal and zero gravity channel flow cases—formulated elsewhere [1,2]—are also presented. The results are important for a qualitative understanding of experiments (see, e.g., [3]) dealing with the behavior of a condenser-section (typically of hydraulic diameters in millimeter or sub-millimeter range). They also relate to issues of better design and integration of condensers needed in ground or space based thermal management systems or power systems—both for large scale (such as Looped Heat Pipes, Capillary Pumped Loops, etc.) and small scale (e.g. electronic-cooling systems) applications.

The classical steady solutions/studies for *external* film condensation flow over vertical, horizontal, and tilted walls ([4–10], etc.) are available and they provide an important test for the numerical solution procedure employed here. A separate paper [11] establishes the ability of the simulation tool to make steady (wave-free) and unsteady (wavy) predictions that are consistent with the well-known results for the classical Nusselt [4] problem.

The simulation tool used here is more completely described in [1,2]. The *interface tracking equation* used here and in [1,2] is the same one that is used for locating the interface in the *interface capturing approaches* for flow with phase-change (level-set method of Son and Dhir [12], etc.) or without phase-change (level-set method of Sussman et al. [13], VOF method of Hirt and Nichols [14], etc.). The *interface tracking approaches* of Esmaeeli and

* Corresponding author. Tel.: +1 906 487 2555; fax: +1 906 487 2822.
E-mail address: narain@mtu.edu (A. Narain).

0017-9310/$ - see front matter © 2006 Elsevier Ltd. All rights reserved.
doi:10.1016/j.ijheatmasstransfer.2005.12.008

Nomenclature

C_{pI}	specific heat (J/(kg K))
h_{fg}	latent heat, $h_g - h_f$ (J/kg)
Ja	Jacob number, $C_{p1}\Delta T/h_{fg}$
k_I	thermal conductivity (W/(m K))
p	pressure at any point (N/m^2)
p_o	pressure at the inlet (N/m^2)
q''_w	bottom wall heat flux at any point and time (W/m^2)
R	tube radius or channel gap (m)
Re_I	Reynolds numbers, $\rho_I U R/\mu_I$
Re_{in}	inlet Reynolds number, Re_2
Re_δ	film Reynolds number, $4\rho_1 u_{1m}\Delta_{steady}/\mu_1$
T_I	temperatures (K)
U	value of the average vapor speed at the inlet (m/s)
u_{1m}	average liquid speed at any x (m/s)
(u_I, v_I)	values of x and y components of velocity at a point (x, y, t) or (x, r, t)—whichever choice is relevant (m/s)
(u_I, v_I)	non-dimensional values of u and v at a point (x, y, t) or (x, r, t)—whichever choice is relevant
(x, y, t)	physical distances (see Fig. 1a) and physical time (m, m, s)
(x, y, t)	non-dimensional values of (x, y, t)
Z_e	ratio of exit vapor mass flow rate to total inlet mass flow rate
ΔT	temperature difference between the vapor and the wall (K)

Greek symbols

π_I	non-dimensional pressure
θ_I	non-dimensional temperature
ρ_I	density (kg/m^3)
μ_I	viscosity (Pa s)
Δ	physical value of condensate thickness (m)
δ	non-dimensional value of condensate film thickness
ν_I	kinematic viscosity, μ_I/ρ_I (m^2/s)
σ	surface tension (N/m)
ε	amplitude of non-dimensional disturbances representing values of $v_1(x, 0, t)$
α	channel/cylinder tilt angle measured from horizontal

Subscripts

I	It takes a value of 1 for liquid phase and 2 for vapor phase
s	saturation condition
w	wall
steady	variable value for the associated steady solution

Superscript

i	value of a variable at an interface location

Tryggvason [15], Juric and Tryggvason [16], Tezduyar [17], Cruchaga et al. [18], etc. also use the same interfacial mass-flux and energy conditions but in somewhat different order and combination. The numerical scheme used here exploits the rigorous analytical and numerical knowledge that exists (see [19]) for solving a reduced hyperbolic form of the *interface tracking equation*—this ensures convergence and accuracy of both the amplitude and the phase of the predicted interfacial waves. Due to an algorithm improvement, the convergence, grid independence, and satisfaction of all interface/boundary conditions for the results reported here are better than what were reported in [1,2].

The laminar/laminar simulation results reported here for common refrigerants and small hydraulic diameter ducts are valid for inlet Reynolds numbers up to 6000 or higher (i.e., $Re_{in} \leqslant 6000$–8000)—this is because, in the vicinity of the interface, the slow liquid condensate laminarizes the vapor flow and one obtains results that are still in a very good agreement with relevant experiments (see [2] for comparisons with channel flow experiments). Furthermore, it has been verified that steady channel and cylindrical simulations are consistent with each other—i.e. the two sets of physical values of steady film thickness are nearly equal when theory and physics demand that they be nearly the same (i.e. the two cases satisfy a specific criteria given in [20]).

The computations predict multiple constrained steady solutions for a range of prescribed steady exit conditions and they also predict, for many cases, a special natural exit condition (selected from a range of choices available at the exit) and the steady flow associated with it. If natural steady/quasi-steady flows exist—as is shown to be the case for gravity dominated or strong shear dominated condensate flows—the computations are also able to predict the approximate values of the critical Reynolds number $Re_\delta|_{cr}$ which marks the transition from stable to unstable behavior of the condensate. The results in this paper suggest a typical range of $Re_\delta|_{cr} \approx 20$–$25$ for laminar-smooth to laminar-wavy transition in the gravity driven flows (which have nearly parabolic condensate velocity profile) and a different range of $Re_\delta|_{cr} \approx 7$–$12$ associated with *loss of parabolicity* instability identified for shear driven (zero gravity or horizontal channel) condensate flows (which typically have linear condensate velocity profile).

The experimental results (presented elsewhere [3]) also clearly support the computational results that show existence of multiple steady solutions for different prescriptions of steady exit conditions and the existence of a special steady

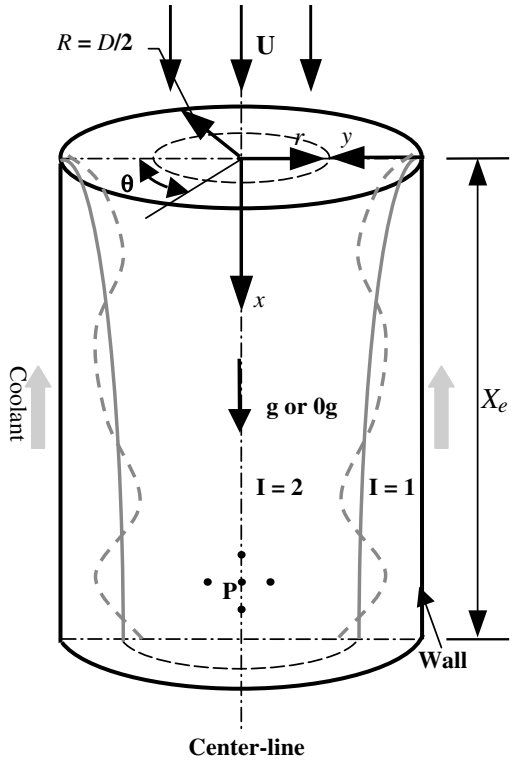

Fig. 1a. Flow geometry of the tube used for simulations.

solution associated with the natural exit condition when no exit condition is prescribed. This *natural* exit condition for unconstrained exit case typically exists only if the flow is *parabolic* up to the exit location for the gravity dominated cases. The simulations, however, also present additional new results for longer length ducts and are able to identify instabilities associated with other *weakly parabolic* to *elliptic* zones. The computations also address some important issues that deal with the role of gravity, surface-tension, and sensitivity to ever-present minuscule wall noise.

Therefore currently available heat transfer correlations ([21,22], etc.) and flow regime maps (see [23,24], etc.) can be improved, by a considered inclusion of the above described issues, towards addressing their reported deficiencies (see [25]).

2. Governing equations and boundary, interface and initial conditions

2.1. Channel flow cases

The governing equations (interior equations, interface conditions, etc.) for the channel flow cases are the same as in [1,2].

2.2. In-tube cases

The liquid and vapor phases in the flow (e.g., see, Fig. 1a) are denoted by a subscript I: I = 1 for liquid and I = 2 for vapor. The fluid properties (density ρ, viscosity μ, specific heat C_p, and thermal conductivity k) with subscript I are assumed to take their representative constant values for each phase (I = 1 or 2). Let T_I be the temperature fields, p_I be the pressure fields, $T_s(p)$ be the saturation temperature of the vapor as a function of local pressure p, Δ be the film thickness, $\dot{m}$ be the local interfacial mass flux, $T_w(x)$ ($< T_s(p)$) be a *known* temperature variation of the cooled cylinder tube wall, and $\mathbf{v}_I = u_I\hat{\mathbf{e}}_x + v_I\hat{\mathbf{e}}_r$ be the velocity fields. Furthermore, let R be the tube radius, g_x and g_y be the components of gravity along x and y axes, p_0 be the inlet pressure, $\Delta T \equiv T_s(p_0) - T_w(0)$ be a representative controlling temperature difference between the vapor and the bottom plate, h_{fg} be the heat of vaporization at temperature $T_s(p)$, and U be the *average* inlet vapor speed determined by the inlet mass flow rate. With t representing the physical time and (x, r) representing physical co-ordinates of a point with respect to the axes in Fig. 1a ($x = 0$ is at the inlet, $r = 0$ is at the center, and $y = R - r = 0$ is at the condensing surface), we introduce a new list of fundamental non-dimensional variables through the following definitions:

$$\{x, y, r, \delta, u_I, \dot{m}\} \equiv \left\{\frac{x}{R}, \frac{y}{R}, \frac{r}{R}, \frac{\Delta}{R}, \frac{u_I}{U}, \frac{\dot{m}}{\rho_1 U}\right\},$$
$$\{v_I, \theta_I, \pi_I, t\} \equiv \left\{\frac{v_I}{U}, \frac{T_I}{\Delta T}, \frac{p_I - p_0}{\rho_I U^2}, \frac{t}{(R/U)}\right\}. \quad (1)$$

2.2.1. Interior equations

The non-dimensional differential forms of mass, momentum (axial and radial components), and energy equations for flow in the interior of either of the phases are well known and are given in Eq. (A.1) of the Appendix.

2.2.2. Interface conditions

The nearly exact interface conditions [26] for condensing flows are given in Appendix Eqs. (A.1)–(A.9) of [1]. Utilizing a superscript "i" for values of flow variables at the interface given by $H \equiv R - r - \Delta(x,t) = 0$, non-dimensional forms of the interface conditions are given below.

- The non-dimensional form of the requirement of continuity of tangential component of velocities (Eq. (A.2) of [1]) becomes

$$u_2^i = u_1^i - \delta_x(v_2^i - v_1^i), \quad (2)$$

where $\delta_x \equiv \partial\delta/\partial x$.

- The non-dimensional form of the normal component of momentum balance at the interface (Eq. (A.3) of [1]) becomes

$$\pi_1^i = \frac{\rho_2}{\rho_1}\pi_2^i - \frac{1}{We}\left(\frac{\delta_{xx}}{[1+\delta_x^2]^{3/2}} + \frac{1}{(1-\delta)\sqrt{1+\delta_x^2}}\right) + \dot{m}^2\left(\frac{\rho_1}{\rho_2} - 1\right), \quad (3)$$

where $We \equiv \rho_1 U^2 R/\sigma$, and surface tension $\sigma = \sigma(T)$ where T is the interfacial temperature. When the

interface is wavy, the equations governing the evolution of superposed disturbances imply, in some cases, a stronger dependence on the surface tension parameter We.

- The tangential component of momentum balance at the interface (Eq. (A.4) of [1]) becomes

$$\left.\frac{\partial u_1}{\partial r}\right|^{i} = \frac{\mu_2}{\mu_1}\left.\frac{\partial u_2}{\partial r}\right|^{i} + [t], \tag{4}$$

where the term [t] used here has a definition given by Eq. (A.2) in the Appendix of this paper.

- The non-dimensional forms $\dot{m}_{LK}$ and $\dot{m}_{VK}$ represent the physical values of non-zero interfacial mass fluxes $\dot{m}_{LK}$ and $\dot{m}_{VK}$ defined in Eq. (A.5) of [1]. These mass fluxes arise from kinematic constraints imposed by normal components of relative velocities of the liquid and the vapor at the interface and are given by

$$\dot{m}_{LK} \equiv \left[u_1^i(\partial\delta/\partial x) - (v_1^i - \partial\delta/\partial t)\right]/\sqrt{1+(\partial\delta/\partial x)^2},$$
$$\dot{m}_{VK} \equiv (\rho_2/\rho_1)\left[u_2^i(\partial\delta/\partial x) - (v_2^i - \partial\delta/\partial t)\right]/\sqrt{1+(\partial\delta/\partial x)^2}. \tag{5}$$

- The term $\dot{m}_{Energy}$ is the non-dimensional form of the non-zero interfacial mass flux $\dot{m}_{Energy}$ that appears in Eq. (A.6) of [1]. It represents the constraint imposed on the interfacial mass flux by the balance equation for energy transfer across the interface. This constraint is given by:

$$\dot{m}_{Energy} \equiv Ja/(Re_1 Pr_1)\{\partial\theta_1/\partial n|^i - (k_2/k_1)\partial\theta_2/\partial n|^i\}, \tag{6}$$

where $Ja \equiv C_{p1}\Delta T/h_{fg}^0$, $h_{fg}^0 \equiv h_{fg}(T_s(p_o)) \cong h_{fg}(T_s(p_2^i))$, and $Pr_1 \equiv \mu_1 C_{p1}/k_1$.

- The interfacial mass balance requires that the net mass flux (kg/m^2/s) at a point on the interface, as given by Eq. (A.7) of [1], be single-valued regardless of which physical process is used to obtain it. The non-dimensional form of this requirement becomes

$$\dot{m}_{LK} = \dot{m}_{VK} = \dot{m}_{Energy} \equiv \dot{m}. \tag{7}$$

It should be noted that negligible interfacial thermal resistance and equilibrium thermodynamics (this includes Eq. 8 below) on either side of the interface are assumed to hold for all x—values at some distance downstream of the origin (i.e., second or third computational cell onwards). Hence, as per discussions leading to Eq. (A.8) in [1], no non-equilibrium thermodynamic model for the interfacial mass-flux $\dot{m}$ is needed as $\dot{m}$ is computed through any of the equalities in Eqs. (5)–(7) once the solution has been obtained. However reasonable initial estimates (from Nusselt [4] solution, etc.) for $\dot{m}$ may be used to start the iterations that lead to converged solutions that are eventually independent of the initial guess for $\dot{m}$.

- The non-dimensional equilibrium thermodynamic restriction on the interfacial temperatures (as given by Eq. (A.8) in [1]) becomes

$$\theta_1^i \cong \theta_2^i = T_s(p_2^i)/\Delta T \equiv \theta_s(\pi_2^i). \tag{8}$$

Within the vapor domain, for the considered refrigerants, changes in absolute pressure relative to the inlet pressure are large enough to affect vapor motion. However, at the same time, they are too small to affect saturation temperatures, which leads to $\theta_s(\pi_2^i) \cong \theta_s(0)$.

2.2.3. Boundary conditions

The well-known boundary conditions at the tube wall and the axisymmetric conditions at the centerline of the tube are given below. They are:

- At the inlet $x = 0$, $0 \leqslant r \leqslant 1$, and at any time t:

$$u_2(0,r,t) = 1 \quad v_2(0,r,t) = 0,$$
$$\pi_2(0,r,t) = 0 \quad \theta_2(0,r,t) = \theta_s(0). \tag{9}$$

- At $r = 1$, the wall of the tube, at any point $0 \leqslant x \leqslant x_e$, and at any time t:

$$u_1(x,1,t) = 0, \quad v_1(x,1,t) = 0, \quad \theta_1(x,1,t) = \theta_w, \tag{10}$$

where $\theta_w \equiv T_w(x)/\Delta T$. For simulations reported here, $T_w(x) =$ constant (see Table 1).

- At $r = 0$, the center line of the tube, at any point $0 \leqslant x \leqslant x_e$, and any time t, we have

$$\left.\frac{\partial u}{\partial r}\right|_{(x,0,t)} = 0, \quad v_2(x,0,t) = 0,$$
$$\theta_2(x,0,t) = \theta_s(0). \tag{11}$$

Furthermore, at the center line, the temperature is at a superheated value close to saturation temperature and this allows the assumption of a nearly constant saturation temperature for the vapor. This is reasonable because effects of superheat ΔT_{sup} in the typical 5–10 °C range lead to very small vapor Jacob numbers $Ja|_V$ ($\equiv C_p|_V \cdot \Delta T_{sup}/h_{fg}(p_o)$, where $C_p|_V$ is the specific heat of the vapor) and hence these effects are negligible.

2.3. Exit conditions

The condenser section, which is of the type shown in Fig. 1a, is typically a *part* of a closed flow loop. For a given vapor-to-wall temperature difference ΔT, inlet mass flow rate $\dot{M}_{in}$, and inlet pressure p_0 (i.e. $\pi_2 = 0$); the flow loop for partial condensation cases may also be designed to provide: (a) an unconstrained or unprescribed exit condition that allows the vapor to flow under its own choice of exit quality (e.g. through the arrangement in Fig. 3 of [3], a range of $\dot{M}_v/\dot{M}_{in}$ values is available at the exit), or (b) a constrained or prescribed exit condition, which may arise from downstream constraints in the flow loop or by active downstream flow control (e.g. a specific value of $\dot{M}_v/\dot{M}_{in}$ at the exit is prescribed through the arrangement in Fig. 2 of [3]).

In what follows, the flow condition at a point P (or a zone) is called "elliptic," if *both* the upstream and downstream neighbors (besides the side neighbors, as in

Table 1
Specification of the reported condensing flows of saturated R-113 (ASHRAE [28]) vapor through the channel and saturated FC-72 (3M Corporation, USA) vapor through the tube

Flow Geometry	Fig. #	p_o (kPa)	$T_s(p_o)$ (°C)	ΔT (°C)	h or R (m)	U (m/s)			
		Re_{in}	Ja	Fr_x^{-1}	Fr_y^{-1}	ρ_2/ρ_1	μ_2/μ_1	We	Pr_1
Cylinder	7a, 12a, 15, 17	77.546	49.5	5	0.0033	0.3			
		917.9	0.06148	0.3666	0.49×10^{-6}	0.0065	0.02189	75.65	10.229
Cylinder	2, 6a—6f, 7b, 12b, 13	77.546	49.5	5	0.0033	0.41			
		1254.6	0.06148	0.1963	0.26×10^{-6}	0.0065	0.02189	75.65	10.229
Cylinder	8b	77.546	49.5	5	0.0033	1			
		3060	0.06148	0.0329	0.44×10^{-7}	0.0065	0.02189	75.65	10.229
Cylinder	8a, 12c, 16	77.546	49.5	5	0.0033	2			
		6120	0.06148	0.0329	0.44×10^{-7}	0.0065	0.02189	75.65	10.229
Channel	9, 10a, 10b, 11, 14a	1254.6	49.5	5	0.004	0.41			
		1200	0.03413	0.2379	0.32×10^{-6}	0.0052	0.0203	67.9	7.37
Channel	7c, 7d	1254.6	49.5	12.5	0.004	0.41			
		1461	0.08422	0.2379	0.32×10^{-6}	0.0052	0.0203	67.9	7.37
Channel	14b	1254.6	49.5	5	0.004	1			
		2922	0.03413	0.04	0.5×10^{-7}	0.0052	0.0203	67.9	7.37

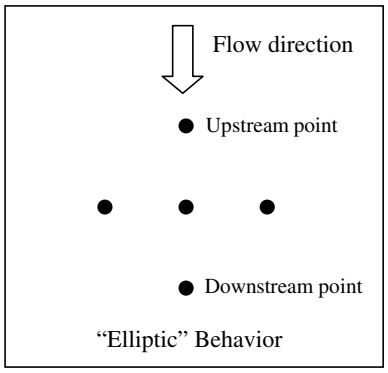

Fig. 1b. "Elliptic" flow condition at point P.

Fig. 1b) affect the value of flow variables at P. The flow condition at a point P (or a zone) is called "parabolic," if *mostly* the upstream and the side neighbors (see Fig. 1c) affect the value of flow variables at P (i.e., the influence of the downstream point is, say, less than 1% of the influence of the remaining points).

The exit condition is specified by specifying the exit pressure or exit vapor quality ratio $Z_e(t)$ at any given time—which is defined as the ratio of vapor mass flow rate at the exit ($x = x_e$) to vapor mass flow rate at the inlet. In general condensing flows are "elliptic" and an exit condition specification leading to compressible or incompressible vapor flow is always possible. For nearly incompressible vapor flows, an expression for $Z_e(t)$ is

$$Z_e(t) = \int_0^{1-\delta(x_e,t)} 2 \cdot r \cdot u_2(x_e, r, t) \cdot dr. \tag{12}$$

For the limited range of prescribed (constrained) *steady* exit conditions considered here, the vapor is nearly *incompressible* and one has, in Eq. (12), $Z_e(t) = \text{constant} = Z_e$. For steady *constrained* (or prescribed) exit condition cases (as experimentally studied by the arrangement in Fig. 2 of [3]), Z_e must be specified with the understanding that if pressure changes with respect to the inlet pressure are not negligible, one must allow for non-uniform but steady values of vapor density.

For *unsteady* flows under *unconstrained* or unspecified exit conditions, a long term natural solution associated with natural exit condition may be possible (i.e., for any steady solution obtained at $t \leqslant 0$ with a prescribed steady exit condition, the unsteady solution yields a natural steady solution as $t \to \infty$). This paper primarily focuses on the unconstrained (or unprescribed) exit condition cases as they are the most commonly occurring situations for condensers in many applications. For practical condensation cases, this means that the value of $Z_e(t)$ in Eq. (12) must not be specified and the "parabolic" and "elliptic" zones of the flow need to be ascertained/deduced by looking at the associated unsteady solution's behavior as $t \to \infty$. A *natural* long term steady value of Z_e (or, equivalently, steady exit pressure)—for a vertical in-tube flow under unconstrained exit conditions (when the exit happens to be in the "parabolic" zone)—is predicted/obtained as in Fig. 2. This is the same approach that has earlier been employed/developed for the vertical channel cases (see [1,2]).

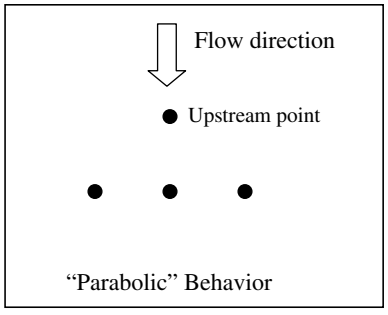

Fig. 1c. "Parabolic" flow condition at point P.

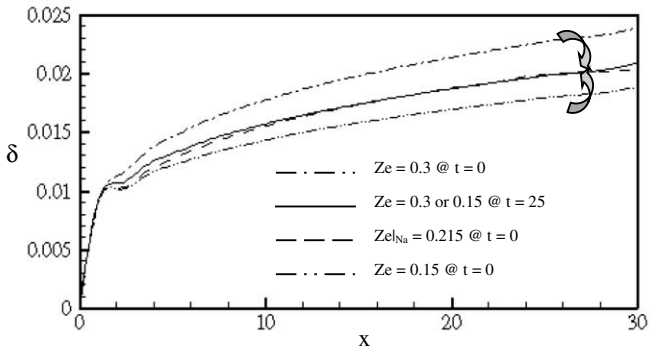

Fig. 2. For tube flow situations specified as in Table 1, the figure depicts two sets of $\delta(x, t)$ predictions for $t > 0$, one curve starts at $Z_e = 0.3$ at $t = 0$, and tends, as $t \to \infty$, to the solution for $Z_e|_{Na} = 0.215$. The other curve starts at $Z_e = 0.15$ at $t = 0$ and tends, as $t \to \infty$, to the same $Z_e|_{Na}$ solution. The spatial/temporal grid-spacings used are, approximately, $(n_i \times n_j) \times \Delta t = (30 \times 50) \times 5$.

2.3.1. Initial conditions

The above described *continuum* equations do not model and incorporate various inter-molecular forces that are important in determining the time evolution of very thin (10–100 nm) condensate film thickness $\delta(x, t)$. As a result, $t = 0$ can not be chosen to be the time when saturated vapor first comes in contact with and condenses on the dry sub-cooled ($T_w(x) < T_s(p_0)$) wall of a tube. With the above modelling limitations, if a steady solution exists, one choice that is often used in this paper is to start at a time ($t = 0$) for which one has a sufficiently thick *steady* solution of the *continuum* equations (where all the governing equations clearly apply) for a prescribed (or constrained) exit condition case—and then, from there, one can obtain the natural large time ($t \to \infty$) steady/quasi-steady solutions with the help of the unsteady equations. That is, if $\phi(x, r, t)$ is any variable (such as u_I, v_I, π_I, θ_I, etc.), the initial values of ϕ and film thickness $\delta(x, t)$ are given as

$$\phi(x, r, 0) = \phi_{steady}(x, r) \quad \text{and} \quad \delta(x, 0) = \delta_{steady}(x), \tag{13}$$

where ϕ_{steady} and δ_{steady} are solutions of the governing equations obtained by dropping all time dependencies in Eqs. (2)–(11) and solving the resulting steady equations (which are *elliptic* near exit) for *any* arbitrarily prescribed steady value of $Z_e(t) = \text{constant} = Z_e$, where:

$$Z_e(0) = \int_0^{1-\delta_{steady}(x_e)} 2 \cdot r \cdot u_2(x_e, r) \cdot dr \equiv Z_e. \tag{14}$$

Although the prescription of the initial Z_e within $0 < Z_e < 1$ is arbitrary, it should be such that it allows a steady computational solution in the stratified/annular regime assumed in Fig. 1a. The long time ($(t \to \infty)$ *natural* steady value of the exit condition (denoted as $Z_e|_{Na}$) associated with a well-defined steady/quasi-steady solution (which exist only if the exit location is within the parabolic zone) under an unconstrained exit condition is independent of the choice of $Z_e = Z_e(0)$ and is computationally found—as noted in the caption for Fig. 2—by the procedure described in [1,2]. More generally, however, as will be seen later, if a long time ($t \to \infty$) steady/quasi-steady solution exists for unconstrained (or unprescribed) exit conditions, this solution may have just a "long term parabolic" steady part or, also, further downstream of it, a poorly defined "long term elliptic" quasi-steady part (with the poor definition arising from the fact that the flow domain and/or arrangement do not specify any exit condition). If the flow is parabolic up to the exit, the $t \to \infty$ "natural" solution is found to be independent of the choice of initial conditions (with Eq. (13) only being a convenient choice).

An inspection of all the non-dimensional governing equations, interface conditions, and boundary conditions reveal the fact that the flows considered here are affected by the following set of 10 independent non-dimensional parameters:

$$\left\{ Re_{in}, Ja, Fr_x^{-1}, \frac{\rho_2}{\rho_1}, \frac{\mu_2}{\mu_1}, Pr_1, x_e, Z_e(0), We \right\}, \tag{15}$$

where $Re_{in} \equiv \rho_2 U R/\mu_2 \equiv Re_2$. Here Re_{in}, $Fr_x{}^{-1}$, and Ja are control parameters respectively associated with inlet speed U, gravity component along x, and temperature difference ΔT. For *unconstrained* exit conditions considered here for which the flow is parabolic up to the exit, Fig. 2 shows that $Z_e(0)$ is an exit condition parameter, which will not affect the long time steady or quasi-steady values of $Z_e(t)$, viz. $Z_e|_{Na}$. For *constrained* exit conditions, e.g. time-averaged $Z_e(t) = Z_e(0)$ or $Z_e(t) = Z_e(0)$ for all $t \geqslant 0$, $Z_e(0)$ is an important flow parameter and its role in defining the possible vapor compressibility effects is not fully understood at present (e.g., if prescribed steady Z_e values are constrained to stay in a range far from $Z_e|_{Na}$ value, vapor compressibility effects may be important). The density ratio ρ_2/ρ_1, viscosity ratio μ_2/μ_1, and Prandtl number Pr_1 are passive fluid parameters. Also, for unsteady wavy-interface situations, particularly in 0g or shear dominated flows, the above equations imply additional dependence on a surface tension parameter, Weber number $We \equiv \rho_2 U^2 R/\sigma$. For superheated vapors, there is a very weak dependence, through Eq. (6), on the thermal conductivity ratio k_2/k_1.

3. Computational methodology

In its broad outline, the computational algorithm and methodology for the in-tube case parallel the algorithm and methodology described in [1,2] for the channel case. However, when compared to the Cartesian channel geometry, there are significant differences in the details of the code for the cylindrical in-tube geometry and these are reported in [27].

4. Flow regime characterizations

There are two types of characterizations of steady/quasi-steady partial condensation flow regimes in a condenser. One type is associated with the prescribed exit conditions

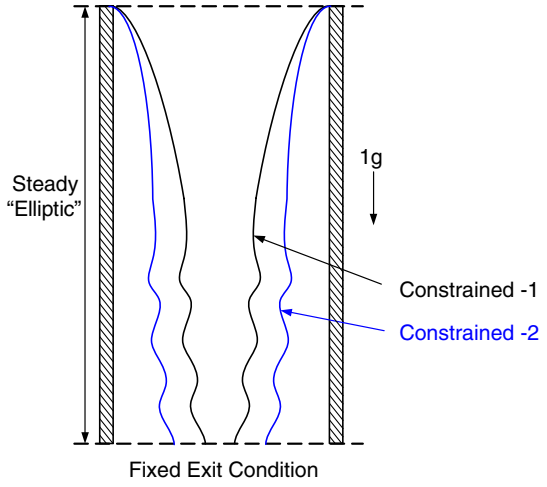

Fig. 3. The computational and experimental results (see [3]) suggest predominantly annular flow regimes for constrained (i.e. prescribed) steady exit conditions.

(i.e. prescribed exit pressure or exit quality $Z_e(t)$) for which the flow inside the condenser is always "elliptic" (see Fig. 3). Therefore changes in the prescription at the exit for a given set of inlet conditions (inlet mass flow rate $\dot{M}_{in}$, etc.) and wall conditions (ΔT, etc.) cause the vapor liquid configuration and the flow inside the condenser to change (with the vapor flow remaining incompressible or becoming compressible). Unlike single phase flows, this "ellipticity" is inherent to internal condensing flows (with prescribed wall temperatures) and it arises from a degree of freedom available through different liquid–vapor configurations (and associated heat transfer rates) that are possible for different vapor flow fields associated with different exit conditions. The realization of different steady/quasi-steady flows for different exit steady condition prescription—as indicated by Fig. 3—is demonstrated—theoretically in this paper and experimentally in another paper [3]. A method for specifying exit condition for partial condensation flows (see the arrangement in Fig. 2 of [3]) gives very stable flows.

The second type of characterization is associated with steady/quasi-steady flows that are some times realized over a long time (often included in start-up time) when no exit conditions are prescribed. This is possible when condenser is placed in a system that allows a suitable range of available choices for exit conditions. For partial condensation, one practical way of achieving steady/quasi-steady flows under unconstrained exit condition is shown in Fig. 3 of [3]. For full condensation cases, a practical way of achieving unconstrained exit condition is described in [3]. In a partial condensation case, as indicated in Figs. 4a and 4b, depending upon the location of the exit, long term steady/quasi-steady regime may consist of either a "parabolic" zone alone or a combination of "parabolic" and "elliptic" zones. By parabolic zone L_P one means that the flow in this zone—with its mass flow rate and temperature difference ΔT—has sufficient "will" to seek its own exit condition unless the conditions at the exit make it impossible to seek this value. Experimental examples of a parabolic flow's "will" to seek its own exit condition and its compatibility or incompatibility with the attainment of steady flow in the components downstream of the condenser are given in [3]. In case of incompatibility, experimental results presented in [3] show occurrence of flow oscillations as a form of system instability. If the exit lies at the end of an elliptic zone; then the flow in the condenser

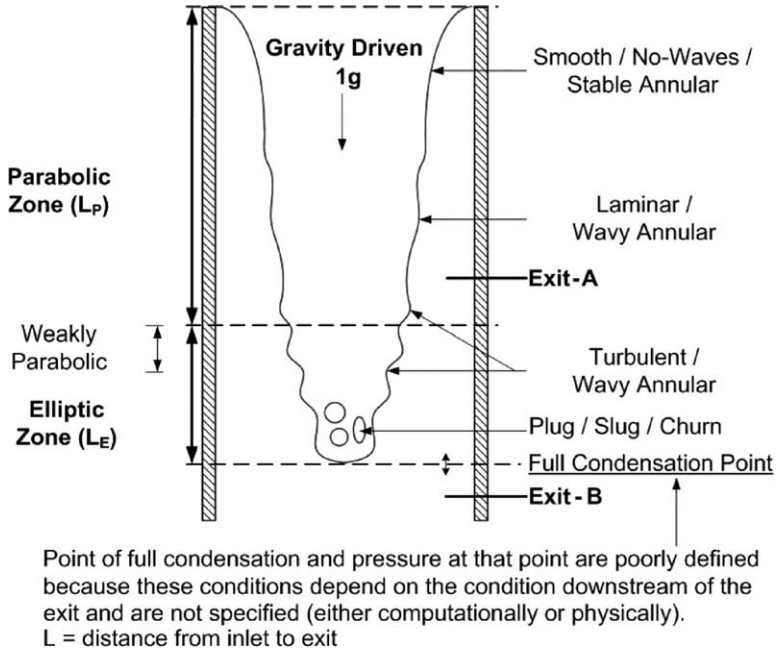

Fig. 4a. Commonly occurring unconstrained (or unspecified) exit-condition cases under normal gravity conditions. Condenser length L is the distance from the inlet to the location of the exit section.

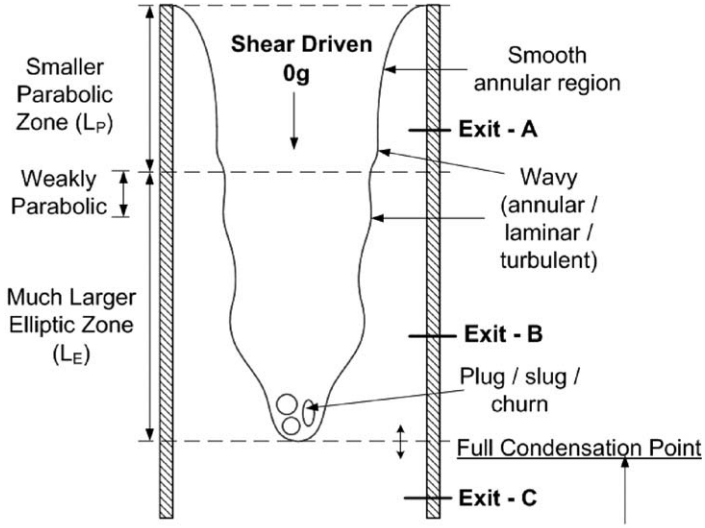

Fig. 4b. Commonly occurring unconstrained (or unspecified) exit-condition cases under shear dominated or zero-gravity conditions. Condenser length L is the distance from the inlet to the location of the exit section.

(and particularly in the elliptic zone) gets determined by the exit condition—whose time dependent (see [3]) or time independent (see [3]) values are strong functions of the system in which the condenser is embedded and pressure constraints or steadiness/stability issues for the flow conditions downstream of the condenser.

However specifying this type of exit condition for a full (or complete) condensation case necessarily involves specification of both the point of full condensation and the value of pressure there. The point of full condensation typically lies in the "elliptic" zone and the exit locations for such cases are characterized by "Exit-B" in Fig. 4a for gravity driven flows and by "Exit-C" in Fig. 4b for shear driven flows. Though it is important, practical ways of specifying different type of exit condition for full condensation case are not straightforward and are being discussed elsewhere.

For full condensation unconstrained cases, if a steady quasi-steady flow exists, the flow zone is typically made up of both "parabolic" and "elliptic" zones (with the one or the other being dominant depending on the value of L_P/L in Figs. 4a and 4b). A method for seeking and achieving an unconstrained steady full condensation case is described in [3].

Typically for shear driven or 0g flows for a given ΔT and no prescribed exit condition, L_P in Fig. 4b decreases with decrease in $\dot{M}_{in}$. However, for gravity driven flows for a given ΔT and no prescribed exit condition, L_P in Fig. 4a may first decrease with $\dot{M}_{in}$ (assuming a large initial value of $\dot{M}_{in}$ for which the vapor shear on the condensate is in the direction of gravity) and then increase again with further decrease in $\dot{M}_{in}$. An increase in L_P with sufficient reduction in $\dot{M}_{in}$ is due to gravity driven condensate's ability to drive the vapor—this is due to the condensate moving significantly faster than the vapor and, as a result, the shear direction on the condensate is, almost everywhere, opposite to the direction of gravity (as in the Nusselt problem [11]).

Computational results are dealt in Sections 5–12.

5. Accuracy and consistency of the numerical method used

The convergence, grid independence, and satisfaction of all the interface/boundary conditions are better (less than 5% in the representative Table 2 for the unsteady wave calculations) than the results reported in [1,2] (which were, on average, less than 6–8% for the most demanding resonant wave calculations). The better accuracy in this paper is because of an improved methodology with regard to the satisfaction of various interfacial mass flux equalities—that are, in this paper, at par with equalities dealing with other interface-conditions. The satisfaction of Eq. (7) is within 3% for all cases except for larger amplitude resonant waves where this equality is typically satisfied within 5% (see Table 2 for a representative case). The spatial and temporal grid spacings and total lengths impose a restriction on wavelength λ and frequency f that can be adequately resolved. If the maximum spacing of the grid in x direction is Δx_m and its total length is x_e while the total time duration is t_e and it is divided in equal intervals of duration Δt; the restrictions imposed by Nyquist criteria [19] are well satisfied for $\lambda \geqslant 4 \cdot \Delta x_m$ and $f \leqslant (4 \cdot \Delta t)^{-1}$ and the restrictions imposed by the domain lengths are well satisfied for $\lambda \leqslant x_e/2$ and $f \geqslant 2/t_e$. The initial ($t = 0$) spatial and

Table 2
Representative interfacial values of relevant non-dimensional variables for the $\lambda = 13$ case (at t = 100) in Fig. 7b

X	$\dot{m}_{LK}$	$\dot{m}_{VK}$	$\dot{m}_{Energy}$	$\pi_1^i + [t]$	π_2^i	u_1^i	u_2^i	τ_1^i	τ_2^i	θ_1^i	θ_2^i
4	1.23E−04	1.23E−04	1.23E−04	−1.76E−02	−1.76E−02	6.60E−02	6.60E−02	4.74E−01	4.74E−01	64.52	64.52
5	1.11E−04	1.11E−04	1.11E−04	−1.73E−02	−1.73E−02	7.59E−02	7.59E−02	3.87E−01	3.87E−01	64.52	64.52
6	1.03E−04	1.03E−04	1.03E−04	−1.71E−02	−1.71E−02	8.45E−02	8.45E−02	3.28E−01	3.28E−01	64.52	64.52
7	9.67E−05	9.68E−05	9.67E−05	−1.68E−02	−1.68E−02	9.26E−02	9.25E−02	2.81E−01	2.81E−01	64.52	64.52
8	9.20E−05	9.20E−05	9.20E−05	−1.66E−02	−1.66E−02	1.00E−01	1.00E−01	2.42E−01	2.42E−01	64.52	64.52
9	8.82E−05	8.82E−05	8.82E−05	−1.64E−02	−1.64E−02	1.08E−01	1.08E−01	2.07E−01	2.07E−01	64.52	64.52
10	8.49E−05	8.49E−05	8.49E−05	−1.62E−02	−1.62E−02	1.15E−01	1.15E−01	1.76E−01	1.76E−01	64.52	64.52
11	8.21E−05	8.22E−05	8.21E−05	−1.60E−02	−1.60E−02	1.23E−01	1.23E−01	1.48E−01	1.48E−01	64.52	64.52
12	7.97E−05	7.97E−05	7.97E−05	−1.58E−02	−1.58E−02	1.31E−01	1.30E−01	1.24E−01	1.24E−01	64.52	64.52
13	7.76E−05	7.76E−05	7.76E−05	−1.56E−02	−1.56E−02	1.38E−01	1.38E−01	1.01E−01	1.01E−01	64.52	64.52
14	7.57E−05	7.57E−05	7.57E−05	−1.54E−02	−1.54E−02	1.46E−01	1.45E−01	7.96E−02	7.96E−02	64.52	64.52
15	7.39E−05	7.39E−05	7.39E−05	−1.53E−02	−1.53E−02	1.54E−01	1.53E−01	5.97E−02	5.97E−02	64.52	64.52
16	7.23E−05	7.24E−05	7.23E−05	−1.51E−02	−1.51E−02	1.61E−01	1.61E−01	4.12E−02	4.12E−02	64.52	64.52

The values show satisfaction of *all* the interface conditions. *Note*: $t = -\frac{1}{We}\left(\frac{\delta_{xx}}{[1+\delta_x^2]^{3/2}}\right) + \dot{m}^2\left(\frac{\rho_1}{\rho_2} - 1\right)$.

temporal grids are defined by ($n_i \times n_j \times n_t$), where n_i is the total number of initial grid points along x (0 to x_e), n_j is the total number of initial grid points along r (0 to 1) or y (0 to 1), and n_t is number of time steps with equal intervals (Δt). Typical values of n_i (and n_j) used for the cylindrical geometry were of the order 20–40 (and 40–60) and for the channel geometry were 30–50 (and 50–70).

A separate paper [11] also establishes the ability of the simulation tool to make predictions that are consistent with the well-known steady/unsteady results for *external* film condensation flows for the classical Nusselt [4] problem.

Furthermore, it has been verified (see Fig. 5) that the channel and cylindrical simulations are consistent—i.e. physical values of steady film thickness are nearly the same when theory and physics demand (see [20]) that they be nearly the same. This criterion, discussed in the Appendix of [20], states that if the channel height h and tube diameter $D = 2R$ satisfy

$$h = D/4 = R/2, \tag{16}$$

and, in addition, when both the channel and the corresponding tube geometries employ the same fluid and have the same values of: duct lengths x_e, inlet pressure, inlet temperature, average inlet speed U, temperature difference ΔT between the vapor and the condensing surface, and exit vapor quality Z_e; then the approximate equality of the average heat transfer coefficients $\bar{h}_x$ is expected for each $x = x_e$. Because of the equality of the average heat transfer coefficients, the approximate equality:

$$\Delta(x)|_{\text{channel}} \cong \Delta(x)|_{\text{tube}}, \tag{17}$$

follows, as is the case for Fig. 5, for all x-locations where liquid temperature profiles are linear across the condensate thickness.

6. Multiple constrained steady solutions

6.1. In-tube/channel cases

As depicted in Fig. 2 for the vertical-tube case and also discussed for various channel cases (see [1,2]), the computations find multiple steady solutions associated with a range of exit conditions. In other words, as generally characterized in Fig. 3, the problem is elliptic and different steady solutions correspond to different steady specifications of

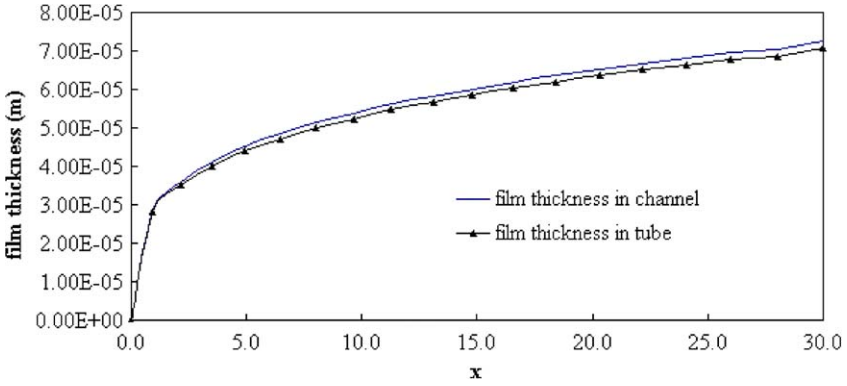

Fig. 5. The above figure compares physical values of film thickness obtained for an in-tube case with a corresponding channel flow case. The two vertical and steady down-flow situations are specified by $h = D/4 = 0.00165$ m, U = 0.41 m/s, $p_o = 77.546$ kPa, $T_s(p_o) = 49.5$ °C, $\Delta T\ (p_o) = 5$ °C and R-113 as fluid. The exit conditions (at $x_e = 30$) are the same, i.e, $Z_{e,\text{channel}} = Z_{e,\text{in-tube}} = 0.3$.

the exit condition (say by the arrangement shown in Fig. 2 of [3]). For all the three constrained steady cases in Fig. 2, the solutions are reasonable as the uniform vapor density approximation still holds. The computations for Fig. 2 also demonstrate, under *unconstrained* exit condition (e.g., as achieved by the arrangement in Fig. 3 of [3]), there exists a "natural" exit condition for many of the vertical in-tube cases. These cases relate to Fig. 4a with the exit being at a location which lies within the long term "parabolic" zone (characterized as "Exit-A" in Fig. 4a). Representative details of these types of steady 1g and 0g natural exit condition solutions are described in Figs. 6a–6f. Fig. 6a shows the trends of the film thickness and the liquid and vapor velocity profiles u_I as a function of y at $x = 10$. Fig. 6b shows the trends of the film thickness and the liquid and vapor temperature profiles θ_I as a function of y at $x = 10$.

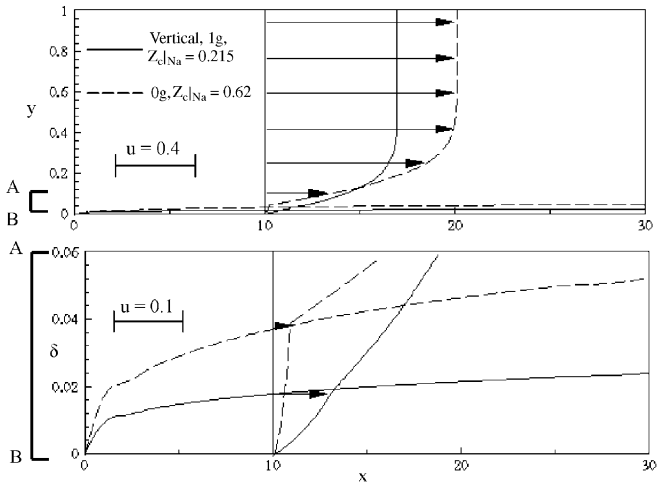

Fig. 6a. For steady in-tube flows under conditions specified as in Table 1 (1g vertical and 0g), the figure shows the u_I-velocity (x-component) profile ($I = 1$ and 2) at $x = 10$ and compares their film thickness values.

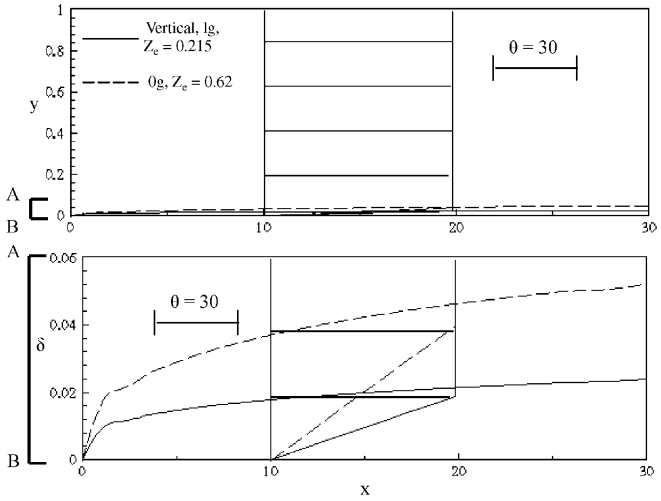

Fig. 6b. The above figure is for the cases considered in Fig. 6a and shows "θ_I ($I = 1$ & 2) versus y" profile at $x = 10$.

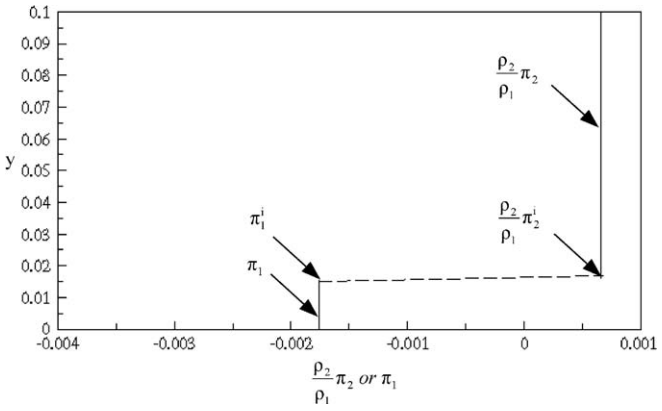

Fig. 6c. The above figure is for the normal gravity case considered in Fig. 6a and shows "π_1 versus y" and "$\frac{\rho_2}{\rho_1}\pi_2$ versus y" profile at $x = 10$.

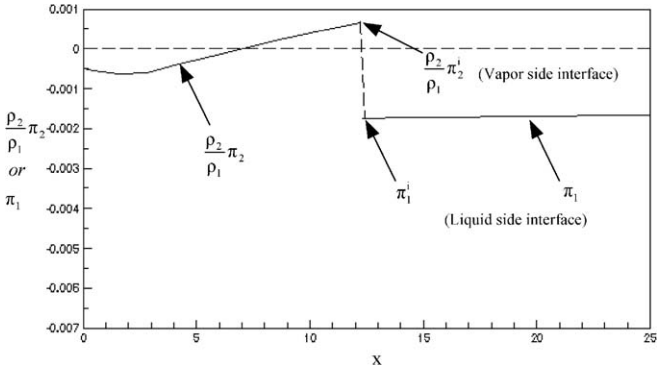

Fig. 6d. The above figure is for the normal gravity case considered in Fig. 6a and it shows "π_1 versus x" and "$\frac{\rho_2}{\rho_1}\pi_2$ versus x" profile at $y = 10$.

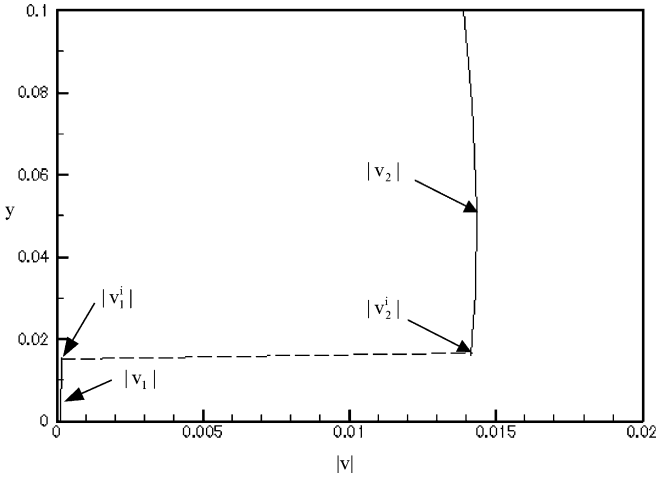

Fig. 6e. The above figure is for the normal gravity case considered in Fig. 6a and shows "$|v_I|$ versus y" for $I = 1$ and 2 at $x = 10$.

As described in the captions for Figs. 6c, 6d, these figures respectively show representative y- and x-profiles of the relevant non-dimensional pressures. Fig. 6e shows the variations in the magnitude of the transverse velocity components v_I for the liquid and for the vapor. Fig. 6f shows

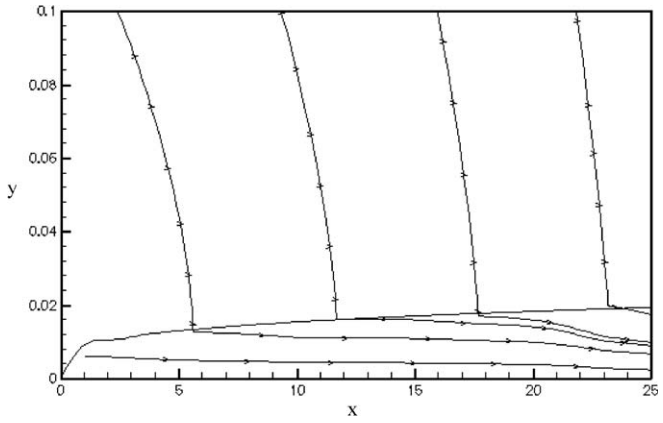

Fig. 6f. The above streamline pattern is for the normal gravity case considered in Fig. 6a.

the representative streamline pattern for a normal gravity case considered in Fig. 6a.

Experiments reported in [3] also clearly confirm the above described results regarding the multiplicity of constrained steady solutions and the existence of a natural exit condition for those gravity dominated partial condensation cases for which the exit lies within the long term "parabolic" zone (such as Exit-A in Fig. 4a). Since the currently available simulation tool does not allow unsteady and non-uniform values of vapor density that are needed for studies that can address realizabilty, stability, and noise-sensitivity issues for the constrained steady solutions; such computational studies are not undertaken here. It should be noted, though, that the experimental results reported in [3] suggest that many of the constrained steady solutions are far more stable/robust than their *natural* exit condition counterparts.

In what follows, the focus of this paper is primarily on the steady/quasi-steady flows the can possibly be achieved under the more commonly occurring unconstrained (unprescribed) exit condition situations. For these cases, assumption of nearly incompressible vapor flows is typically good. The paper further focuses on an investigation of realizabilty, stability, and noise-sensitivity of such flows.

7. Stability issues

These studies look at the long term response of solutions when: (i) different wave-length sinusoidal disturbances are superposed at various locations of the initial film thickness profile, and (ii) no initial disturbances (except those that may arise from the numerical approach) are superposed on the initial data. The "no initial disturbance" study helps in determining the zones of "parabolicity" and "ellipticity" within the condenser. For example, at $t = 0$, if one goes from prescribed exit condition $Z_e(t) = Z_e(0)$ for $t \leqslant 0$ to unspecified $Z_e(t)$ values at $t > 0$, the "no initial disturbance" study is best suited for identifying multiple drifting solutions (with multiplicity arising from different initial choices of $Z_e(0)$ for different exit conditions) in the elliptic zone L_E of Figs. 4a and 4b and, also, for identifying nearly identical long term solutions for the parabolic zone L_P of Figs. 4a and 4b.

7.1. Gravity driven cases

7.1.1. In-tube geometry

The stability response of smooth-interface steady solutions associated with *natural* exit-condition (such as the normal gravity solution in Fig. 2) is investigated in Figs. 7a and 7b for the in-tube flows. It is found that, for the representative case considered in Fig. 7a, the normal gravity solutions are stable (i.e., amplitudes do not grow) over

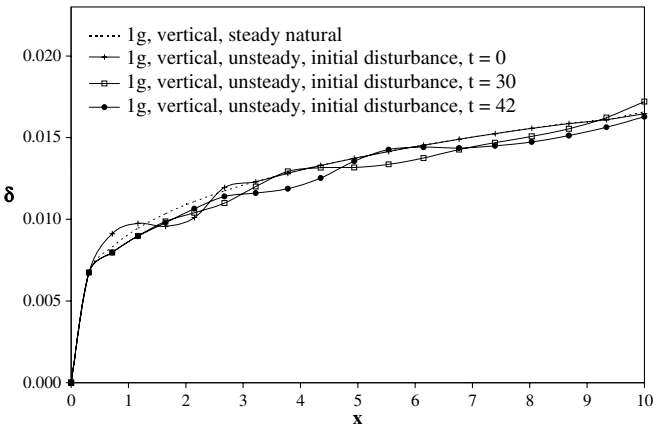

Fig. 7a. For flow situations specified in Table 1 of the tube, the above film thickness predictions ($\Delta t = 1$) are for a vertical tube under normal gravity conditions. An initial disturbance on the steady film thickness solution was superposed at $t = 0$ and tracked to $t = 42$. The initial δ is given as $\delta(x, 0) = \delta_{steady}(x) + \delta'(x, 0)$, where a non-zero disturbance $\delta'(x, 0)$ was given at $t = 0$ on the steady solution δ_{steady}. Here $\delta'(x, 0) = 0.0015 \cdot \sin(2\pi x/\lambda)$ for $3.5 \geqslant x \geqslant 0.3$ and $\lambda = 2.6$.

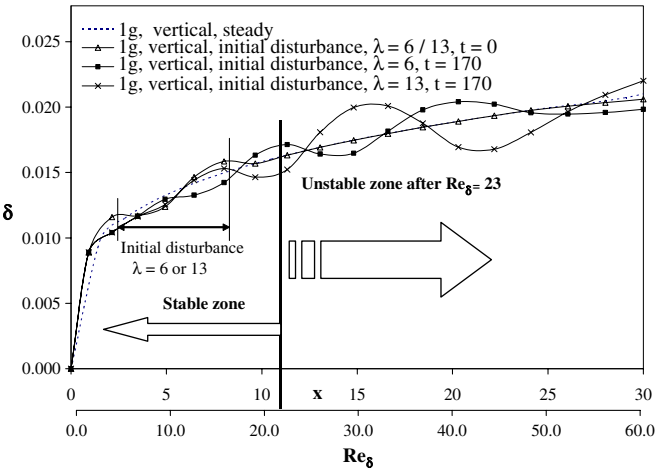

Fig. 7b. For flow situations specified in Table 1 of the tube, the above film thickness predictions ($\Delta t = 5$) are for a vertical tube under normal gravity conditions. An initial δ on the steady film thickness solution was superposed at $t = 0$ and tracked to $t = 170$. The initial disturbance is given as $\delta(x, 0) = \delta_{steady}(x) + \delta'(x, 0)$, where a non-zero disturbance $\delta'(x, 0)$ was given at $t = 0$ on the steady solution δ_{steady}. Here $\delta'(x, 0) = 0.001 \cdot \sin(2\pi x/\lambda)$ for $9.5 \geqslant x \geqslant 0.9$ and $\lambda = 6$ and 13.

the length of the tube for which $x \leqslant 10$ and $Re_\delta \leqslant 22$. However, for the longer length tubes in Fig. 7b, there is a loss of stability, i.e., amplitudes are eventually sufficiently large—which is defined here to mean that they are more than 2.5 times the amplitudes of the initial sinusoidal disturbance and, at the same time, greater than 15% of the initial undisturbed film thickness at their long time locations. By definition, initial sinusoidal disturbance are required to have locations near the inlet and amplitudes that are less than 10% of the undisturbed film thickness near the inlet. Under the above definition, the longer length flows lose stability for $Re_\delta \geqslant Re_\delta|_{cr} \approx 23$. This loss of stability for the gravity driven forced internal flow still keeps the exit within the long term parabolic zone (as characterized by "Exit-A" in Fig. 4a). The instability is qualitatively similar (though somewhat different quantitatively) to the one found for the gravity driven Nusselt problem [4] for which we have shown (see [11]) that $Re_\delta|_{cr} \approx 30$—a well-known estimate which is also supported by experiments. These steady solutions—including the stable zones—are quite *noise-sensitive* (as seen below through Figs. 12a and 12b), thereby making their actual realization only a quasi-steady phenomenon. The instability at $Re_\delta|_{cr} \approx 23$ appears to be associated with the fact that gravity speeds up the thin-film condensate flows and, therefore, is perhaps associated with Tollmien-Schlichting type instability (increasing film Reynolds number Re_δ) in the presence of free-surface wave phenomena and mass transfer across the interface.

7.1.2. Channel geometry

The cases for flow through a short length channel ($Re_\delta \leqslant 2$) follow the stability trends described in [1,2]. The longer length cases follow the in-tube case trends described in Figs. 7a and 7b. For example, in Fig. 7c, the channel analogue of the case in Fig. 7b is shown. This instability (at locations where $Re_\delta \geqslant 30$), because of high growth rates of computational noise and proximity to the "elliptic" zone (see the characterization in Fig. 4a), also manifests itself in Fig. 7d that deals with the case for no initial disturbances.

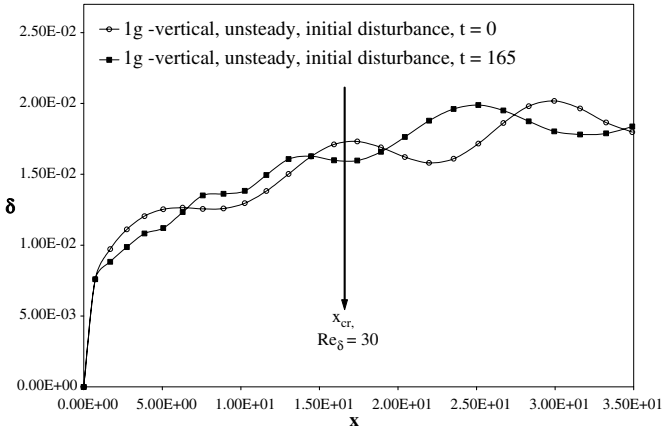

Fig. 7c. For flow situations specified in Table 1 of the channel, the above film thickness predictions ($\Delta t = 3$) are for a vertical channel under normal gravity conditions. An initial disturbance on the steady film thickness solution was superposed at $t = 0$ and tracked to $t = 165$. The initial δ is given as $\delta(x, 0) = \delta_{steady}(x) + \delta'(x, 0)$, where a non-zero disturbance $\delta'(x, 0)$ was given at $t = 0$ on the steady solution δ_{steady}. Here $\delta'(x, 0) = 0.001 \cdot \sin(2\pi x/\lambda)$ for all x and $\lambda = 13$. The interface was tracked with $\Delta t = 3$.

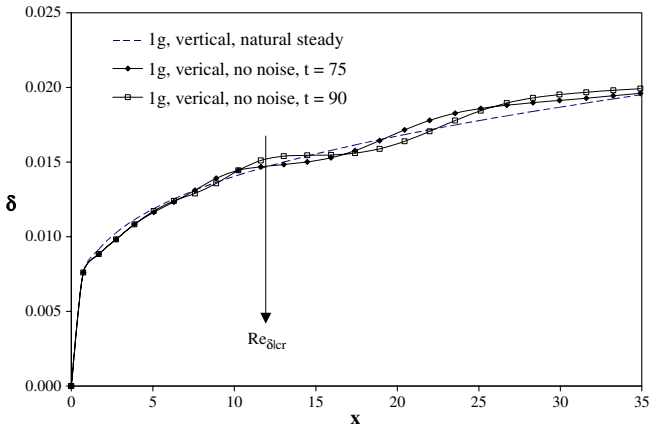

Fig. 7d. For flow situations specified in Table 1 of the tube, the above film thickness predictions ($\Delta t = 15$) are for a vertical channel under normal gravity conditions exposed to no noise condition.

7.2. Shear driven cases

7.2.1. In-tube geometry

Fig. 8a results for a 0g in-tube flow show stability because the shear driven flow has a sufficiently strong interfacial shear (i.e. neither weak nor so strong that it can destabilize the flow) through out the "long term parabolic" zone associated with the chosen inlet vapor speed, temperature difference ΔT, and the length of the duct (with unconstrained exit conditions). As the inlet vapor speed is reduced, as is the case in Fig. 8b, there are instabilities associated with the long term "weakly-parabolic/elliptic-zone" that the vapor must enter after its passage through the

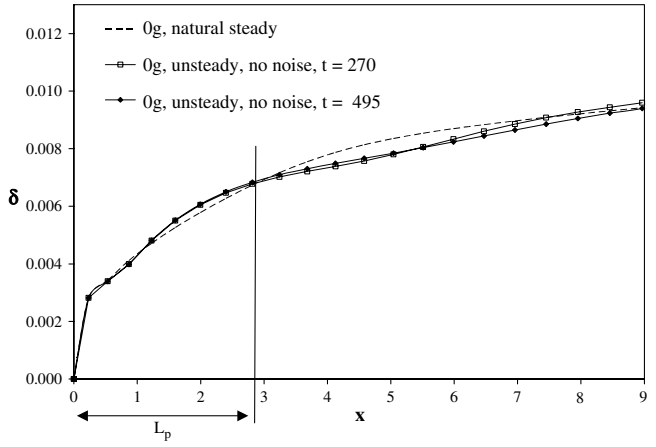

Fig. 8a. For flow situations specified in Table 1 of the channel, the above film thickness predictions ($\Delta t = 3$) are for a channel under zero-gravity conditions and exposed to no externally imposed noise.

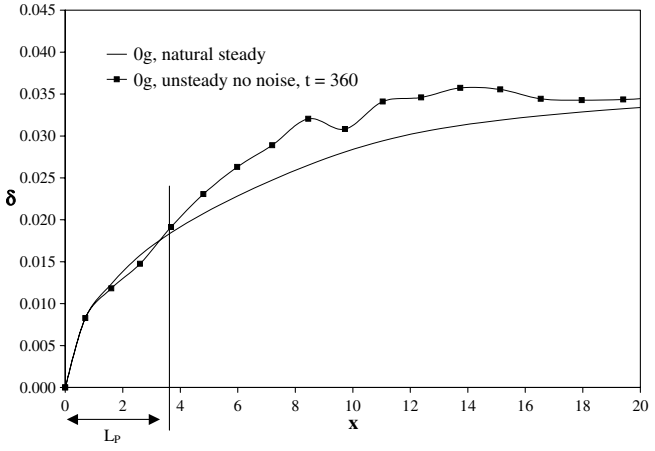

Fig. 8b. For in-tube (zero gravity) flow situation specified as in Table 1, the figure above shows the effects of inadequate shear and associated convective instabilities of the steady solutions (t = 0). The interface was tracked with Δt = 15.

parabolic zone (exit location is characterized by "Exit-B" in Fig. 4b). These shear driven flow instabilities are described below, in greater details, for the channel geometry case.

7.3. Channel geometry

As do the results for the in-tube cases of Fig. 8a, Fig. 9 results for a horizontal channel flow (also see [1,2]) show that the basic natural steady flow is stable to initial disturbances. However, the existence of this stable and *natural* steady solution (unconstrained exit) for this particular shear driven flow is a result of the fact that the "long term parabolic" vapor flow zone covers the short length of the duct (the exit location is characterized by "Exit-A" in Fig. 4b). This is also because the inlet vapor speed is sufficiently large and the temperature difference ΔT is sufficiently small. For longer channel-length cases (dealing with horizontal channel or zero gravity configurations) considered in Figs. 10a and 10b—at locations where vapor shear is inadequate to drive the condensate—there is, however, a sufficiently strong instability that is noticeable even in the absence of initial disturbances or wall noise. The fact that this static type convective instability arises in the seeking of a "natural" exit condition from a prescribed initial condition indicates that a natural exit condition—in the sense of an *attractor* solution defined in Liang et al. [2] with the help of Fig. 4 in [2]—does not exist when the vapor flow slows down enough to make its long time governing equations behave "weakly parabolic" to "elliptic" as opposed to "parabolic." This means that this exit location of condenser is characterized by "Exit-B" in Fig. 4b. In fact it can be said that, over the parabolic zones, shear driven cases in 0g have *attractors* (steady flow solutions) that are often quite weak in the sense that the long term steady

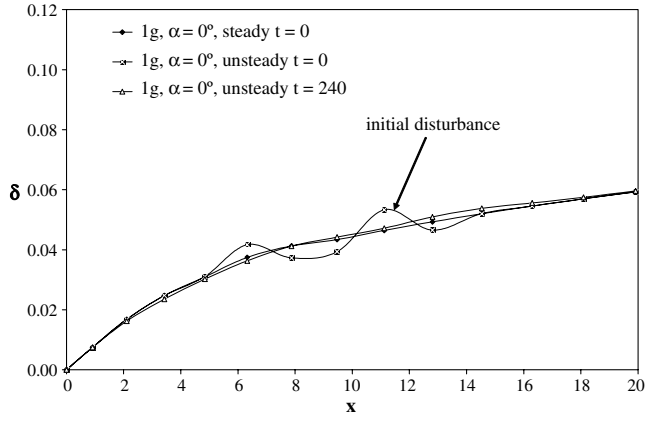

Fig. 9. For horizontal channel (normal gravity) flow situation specified in Table 1, the above figure shows the stable response (at t = 240) of transient film thickness to an initial disturbance ($\delta(x,0) = \delta_{steady}(x) + \delta'(x,0)$) shown at t = 0. The interface was tracked with Δt = 10.

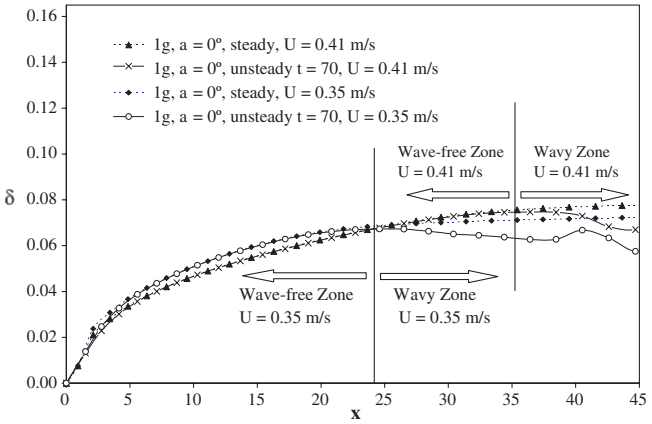

Fig. 10a. For horizontal channel (normal gravity) flow situation specified as in Table 1, the figure above shows the effects of inadequate shear and associated convective instabilities of the steady solutions (t = 0) under no noise conditions. The interface was tracked, in the absence of any initial disturbance, with Δt = 10.

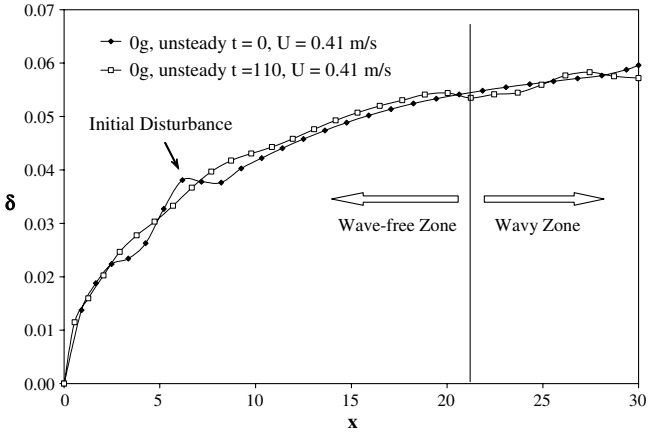

Fig. 10b. For channel (zero gravity) flow situation specified as in Table 1, the above figure removes gravity (i.e. 0g) from the U = 0.41 m/s case considered in Fig. 7a. The figure shows the effects of initial disturbance in the stable parabolic and unstable elliptic portions of the flow. The interface was tracked with Δt = 10.

flows are only neutrally stable under unconstrained exit conditions—that is, they show small drifting for small initial disturbances (implying that the bottom point of the suggested bowl in Fig. 4 of [2] is no longer a point but rather a set of points that resemble a flat surface—this is because the exit location has shifted from being in a "parabolic zone" to being in a "weakly parabolic" zone). This behavior summarized as "Exit-B" behavior in Fig. 4b, corresponds to attaining a naturally selected steady solution over the parabolic zone and attaining a rather indeterminate solution (prone to disturbances and can only be repeatedly realized to within 10-15% of a certain solution) over the "weakly parabolic" zone. The above described "loss of parabolicity" phenomenon associated with the convective instabilities in Figs. 10a and 10b are also accompanied by the typical instabilities associated with the amplification of initial disturbances in this wavy zone. Therefore, the condensate, in general, will not achieve a wave-free steady solution over this downstream part of the duct length. As is shown in Fig. 10b, the downstream "elliptic" zones are quite sensitive to initial disturbances while the upstream wave-free zones are not. The disturbances in the upstream small amplitude wave zone are simply propagated forward into the downstream large amplitude wave zone. Furthermore, as shown in Fig. 10a, as the inlet speed U is reduced, the wave-free leading edge "parabolic" zone in the front shrinks further and, eventually, one may not have *any* wave free zone (associated with a natural steady solution) for the flow. That is, for shear driven zero-gravity or horizontal channel flows, quasi-steady (i.e. steady-in-the-mean) flows can not *always* be realized because the inadequacy of the available shear may not allow existence of a natural exit condition and this makes, in the long term, part or all of the flow "elliptic" and *unstable* or *unidentifiable* under unconstrained exit conditions.

In summary, the stability for shear driven condensate is significantly weaker than normal gravity on four counts: (i) the waves damp out slower, (ii) $Re_\delta|_{cr} \approx 7$–$12$ as opposed to the gravity driven flows' $Re_\delta|_{cr} \approx 20$–$25$, (iii) there may not be a crisp or sharp "natural" exit condition because of the extreme shortness of the long-term "parabolic" zone—thereby making the attractor associated with the natural exit condition only "weakly parabolic" (see the zone characterizations in Fig. 4b), and (iv) a much greater sensitivity of the flows to small changes in the exit condition (pressure or vapor quality) is found because there is a freedom to choose different exit conditions (this is because small changes in exit pressure strongly affect the vapor motion and, in turn, the shear driven liquid motion).

In the light of the above, shear driven steady/quasi-steady partial condensation flow cases (when they exist) in zero-gravity are best realized—with significant suppression of the above described instabilities—by prescribing the exit condition, for example, by arranging the flow downstream of the condenser to operate in a way that fixes the exit condition (e.g., the arrangement in Fig. 2 of [3] gives very stable flows). This constrained situation is more stable than the unconstrained exit condition situation that is more commonly used (e.g., by the arrangement shown in Fig. 3 of [3]).

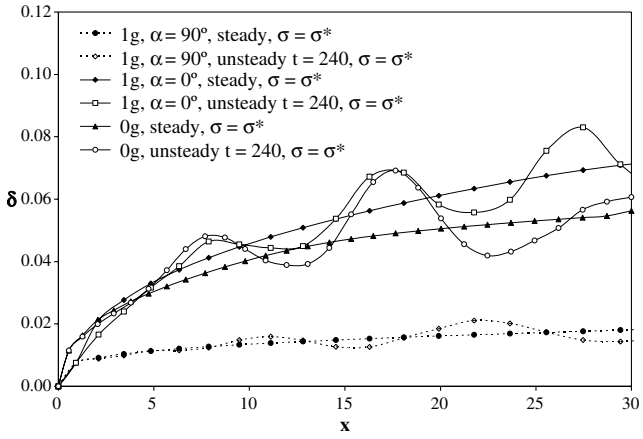

Fig. 11. For channel flow situations specified as in Table 1, the figure above shows the film thickness values for steady no-noise and unsteady resonant bottom wall noise cases—under both zero-gravity and normal gravity environments. Resonant bottom wall noise is given as $v_1(x, 0,t) = \varepsilon \cdot \sin(2\pi x/\lambda) \cdot \sin(2\pi t/T)$, $\varepsilon = 0.75E{-}05$, $\lambda = 10$, and $T(x) = \lambda/\bar{u}_{steady}$. The interface was tracked with $\Delta t = 2.5$ for 1g vertical and $\Delta t = 10$ for 0g and 1g horizontal cases.

8. Effects of gravity on *natural* steady solutions

8.1. Channel geometry

For short length channels ($Re_\delta \leqslant 10$), the results and discussions for 1g versus 0g cases are similar as discussed in [1,2]. The steady results are also compared in Fig. 11. For longer length shear driven channel flows in Figs. 10a and 10b, in comparison to a corresponding gravity driven case, the non-existence of a "natural" solution and/or stability issues for the associated steady/quasi-steady solutions become more critical because of a much smaller length L_P of the long term "parabolic" zone (as compared to gravity dominated cases).

8.2. In-tube geometry

The in-tube results comparing gravity driven (1g) and shear driven (0g) situations—for short length ducts—follow the results given earlier in Figs. 6a–6f.

The in-tube results for 1g and 0g—for longer length ducts—follow the remarks made earlier for Figs. 7b and 8b.

9. Noise-sensitivity of *natural* steady solutions

9.1. Gravity driven cases

9.1.1. In-tube/channel geometries

Despite the stability of short length in-tube condensing flows considered in Fig. 7a, it is found that these flows

(with $Re_\delta \leqslant 22$)—like their channel flow counterparts in 1g or 0g (Fig. 11)—are quite sensitive even to *minuscule* transverse vibrations of the condensing surface (see Fig. 12a). As in [1,2], the standing wave vibrations of the condensing surface are modeled by the velocity boundary condition $v_1(x, 0, t) = \varepsilon \cdot \sin(2\pi x/\lambda) \cdot \sin(2\pi t/T)$ whose amplitude ε is in the range of 10^{-6}—5×10^{-5}, wave-length λ typically produces waves of similar wave-lengths (this is found to be the case over the stable film flow zones considered here), and time period T (frequency $f = 1/T$) may be a given constant or may have a prescribed variation with x. A small amplitude noise is called *resonant* or *non-resonant* depending on whether it does or does not satisfy the resonance criteria given by (also see [11] and Eq. (8) of [2])

$$\lambda \cdot f = \lambda/T(x) = \bar{u}(x,t) \cong \bar{u}_{steady}(x), \tag{18}$$

where $\bar{u} \equiv u_1^i + \{Ja/(Re_1 \cdot Pr_1)\}\partial\theta_1/\partial x|^i$ and $\bar{v} \equiv v_1^i + \{Ja/(Re_1 \cdot Pr_1)\}\partial\theta_1/\partial y|^i$. When the resonance condition in Eq. (18) is satisfied, the forward phase-speed associated with the bottom wall noise coincides with the forward phase-speeds $(\bar{u}(x,t) \cong \bar{u}_{steady}(x))$ associated with the small-amplitude interface waves.

Clearly the results in Fig. 12a show that the resonant noise enhance the wave-effects for the vertical in-tube case just as they do for the channel cases (see [1,2]). The enhancement in the longer tube case of Fig. 12b is clearly greater beyond the location where the steady solution was found to be unstable (i.e., at these locations in Fig. 7b, the amplitudes of waves were much bigger than 15% of the initial undisturbed film thickness).

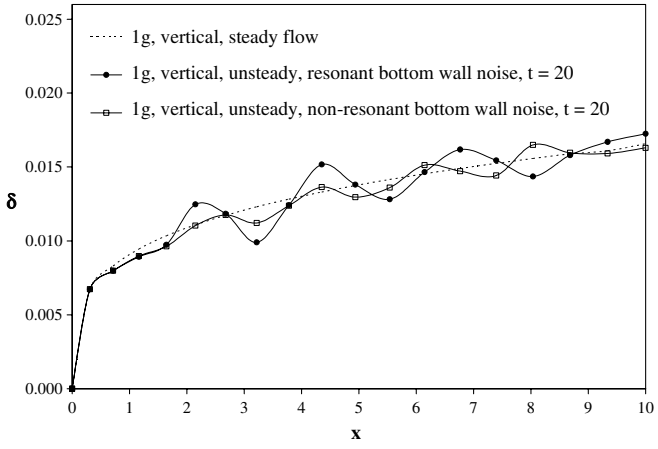

Fig. 12a. For flow situations specified in Table 1, for vertical tube in normal gravity, the figure shows the film thickness values for steady noise-free, unsteady resonant and unsteady non-resonant bottom wall noise cases. Bottom wall noise is given as $v_1(x, 0,t) = \varepsilon \cdot \sin(2\pi x/\lambda) \cdot \sin(2\pi t/T)$, $\varepsilon = 0.5E{-}04$, $\lambda = 2.6$ and $T(x) = \lambda/\bar{u}_{steady}$ for resonant bottom wall noise case while $T = 10$ for non-resonant bottom wall noise case. The interface was tracked with $\Delta t = 1$.

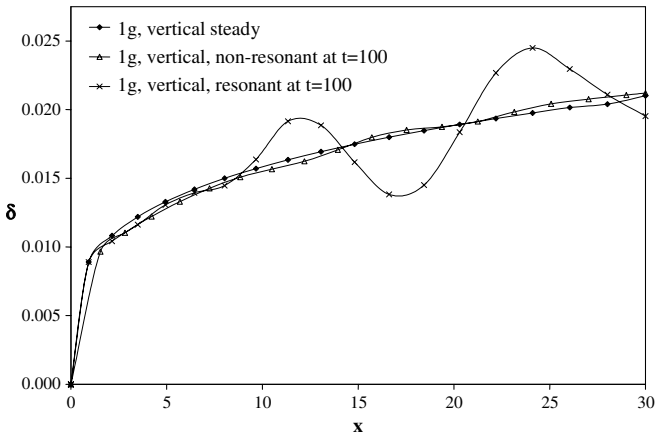

Fig. 12b. For flow situations specified in Table 1 of the longer length vertical tube, the figure above shows the film thickness values for steady noise-free, unsteady resonant and unsteady non-resonant bottom wall noise solution for flow under normal gravity cases. Bottom wall noise is given as $v_1(x,0,t) = \varepsilon \cdot \sin(2\pi\ x/\lambda) \cdot \sin(2\pi t/T)$, $\varepsilon = 0.5E{-}05$, $\lambda = 13$ and $T = T(x) = \lambda/\bar{u}_{steady}$ for resonant bottom wall noise case while $T = 10$ for non-resonant bottom wall noise case. The interface was tracked with $\Delta t = 5$.

9.2. Shear driven cases

9.2.1. In-tube/channel geometries

The complex stability response for shear driven cases as described earlier also determines their noise sensitivity response. The horizontal channel's noise-sensitivity depicted in Fig. 11 is for the stable short-length zone. Therefore the response of the stable wave-free zones to noise (for 0g/horizontal cases in Figs. 10a,10b) shows a persistence of waves (whose amplitudes do not grow) and slight drifting of the mean steady solution. For the downstream unstable wavy zones of Figs. 10a,10b (growing amplitude waves), the behavior in response to a persistent bottom wall noise is one of much larger amplitude waves. Similar, but more sensitive, noise response for 0g in-tube case is shown in Fig. 12c – where, again, the "parabolic" vapor zone is very small.

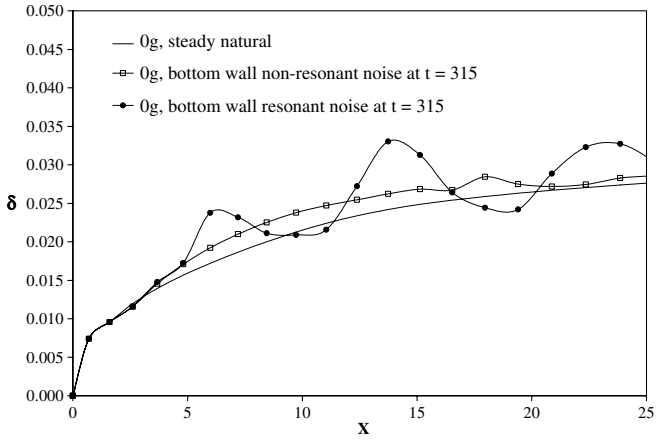

Fig. 12c. For flow situations specified in Table 1, the figure above shows the film thickness values for steady noise-free, unsteady resonant and unsteady non-resonant bottom wall noise solution for the longer length tube under zero gravity. Bottom wall noise is given as $v_1\ (x, 0,t) = \varepsilon \cdot \sin(2\pi x/\lambda) \cdot \sin(2\pi t/T)$, $\varepsilon = 0.35E{-}05$, $\lambda = 8$; with $T = T(x) = \lambda/\bar{u}_{steady}$ for resonant bottom wall noise case while $T = 32$ for non-resonant bottom wall noise case. The interface was tracked with $\Delta t = 15$.

10. Effects of surface tension

10.1. Gravity driven cases

10.1.1. In-tube/channel geometries

An assessment of the role of the surface tension term in the solutions obtained for Figs. 11, 13, and 14a is accomplished by looking at the size of the surface-tension term on the right side of Eq. (3) relative to the size of π_1^i on the left side of Eq. (3). For normal gravity flows—be it in-tube or vertical/horizontal channel—this term is less than 1% for all cases considered thus far. Therefore surface tension value (its presence or absence within a feasible range) is not very important for the gravity driven flow in Fig. 13. Its presence or increase only causes a slight thinning of the mean film thickness and also shows a slight stabilizing effect on the wave amplitudes (they are smaller).

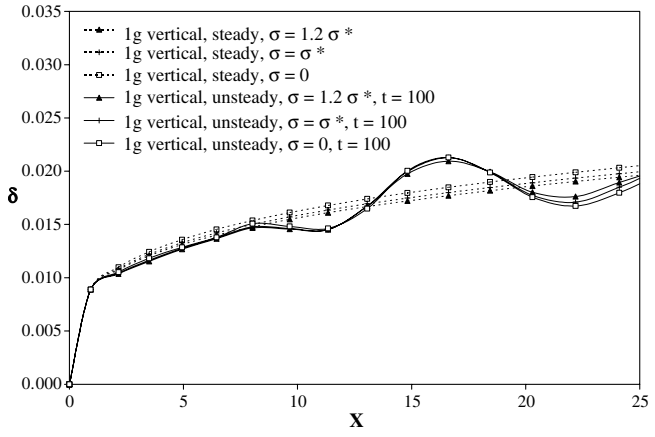

Fig. 13. For the in-tube flow situations specified in Table 1, the above steady and unsteady δ(x,t) values are for the flows with and without natural surface tension of the fluid. The noise is resonant with $v_1(x,0,t) = \varepsilon \cdot \sin(2\pi x/\lambda) \cdot \sin(2\pi t/T)$, $\varepsilon = 0.5E{-}05$, $\lambda = 10$, and $T = T(x) = \lambda/\bar{u}_{steady}$. The interface was tracked with $\Delta t = 5$.

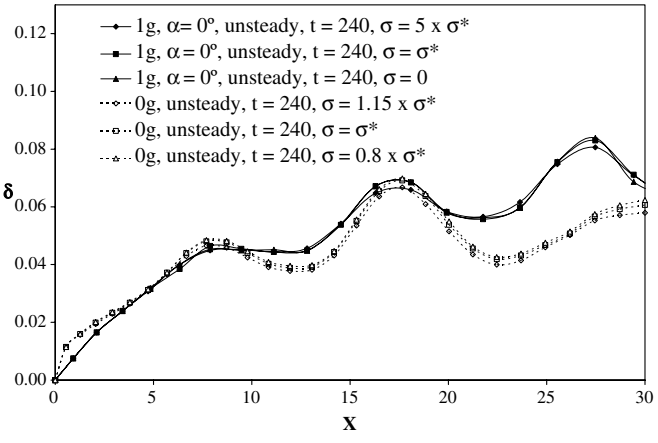

Fig. 14a. For channel flow situations specified as in Table 1, the figure above shows the effect of surface tension on film thickness (at $t = 240$ using $\Delta t = 10$) under zero-gravity and horizontal normal gravity environments. The bottom wall noise is resonant with $v_1(x,0,t) = \varepsilon \cdot \sin(2\pi x/\lambda) \cdot \sin(2\pi t/T)$, $\varepsilon = 0.75E{-}05$, $\lambda = 10$, and $T(x) = \lambda/\bar{u}_{steady}$. The interface was tracked with $\Delta t = 10$.

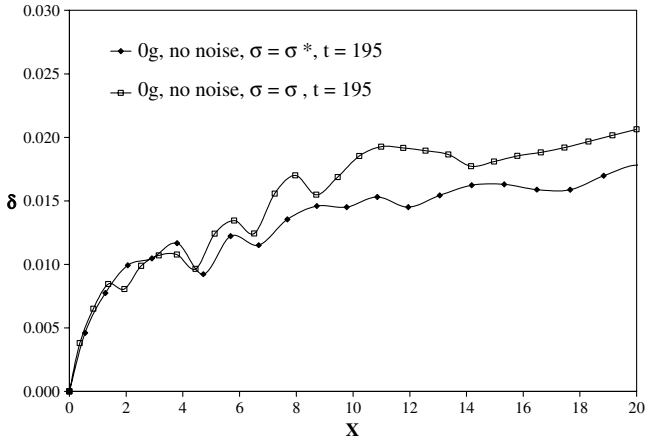

Fig. 14b. For channel flow situations specified as in Table 1, the figure above shows the effect of surface tension on film thickness (at $t = 195$ using $\Delta t = 15$) under zero-gravity environment and no noise condition.

10.2. Shear driven cases

10.2.1. In-tube/channel geometries

However, for zero gravity channel flows, for the cases that have been considered here (fluid is R-113), this term can be as big as 60% for wave-free cases and as big as 300% for resonant wavy cases. And, in fact, for the slow inlet speed ($U = 0.3$ m/s) 0g channel case in Fig. 14a, no steady/quasi-steady solution can be found if surface tension is too small (i.e., for the hypothetical $\sigma = 0$ case). For the higher shear ($U = 1$ m/s) 0g channel cases in Fig. 14b, however, there is an improved ability to withstand waves under absence/reduction of surface tension (i.e. a solution exists for $\sigma = 0$ case). Overall, for shear dominated flows over the parabolic zone for which a natural steady/quasi-steady "parabolic" solution exists and also over the "elliptic" zone of Fig. 14b, it is found that the presence of surface tension or increase in surface tension stabilizes the waves (reduced amplitudes).

The above set of results suggests a need for a more refined and systematic parametric study of the role of surface-tension for zero-gravity flows. In any case, stabilizing condensate flows in zero-gravity by suitable arrangements that prescribe or limit the exit condition values appear to be far more attractive than stabilizing the unconstrained exit flows by manipulating the normal stress or surface tension conditions at the interface.

11. Effects of waves on heat transfer rates

11.1. Gravity driven cases

11.1.1. In-tube/channel geometries

The wave effects for the in-tube cases are found to be quite similar to the channel case [2] and the discussions

given there also apply here. For example, as shown in Fig. 15, for resonant noise, short-length, vertical in-tube cases; there is a 5–10% enhancement in time averaged wall heat flux at large x. Fig. 15 also shows that wall heat flux is slightly larger than the interfacial heat flux for the no-noise steady cases—the difference between the two contributes to the slight subcooling of the condensate as it moves forward. However, for the wavy cases, at some large x segments, the interfacial heat flux may exceed the wall heat flux.

11.2. Shear driven cases

11.2.1. In-tube/channel geometries

For the stable portion of 0g/horizontal internal condensing flows, it is found, as in [2] for channel cases and in Fig. 16 for in-tube cases, there is no significant enhancement in heat transfer rates due to interfacial waviness. In fact, on average, compared to the smooth-interface case, there is a decrease in heat-flux.

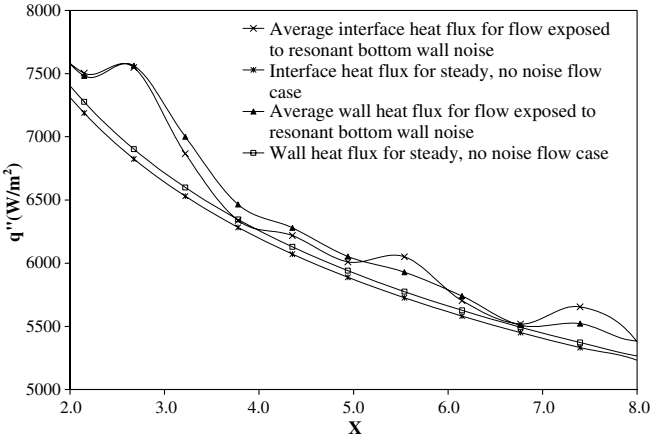

Fig. 15. For flow situations specified in Table 1 for a vertical tube, the figure shows steady and time-averaged values of heat flux at the wall and at the interface. The noise is resonant with $v_1(x, 0,t) = \varepsilon \cdot \sin(2\pi x/\lambda) \cdot \sin(2\pi t/T)$, $\varepsilon = 0.5E{-}04$, $\lambda = 2.6$, and $T = T(x) = \lambda/\bar{u}_{steady}$.

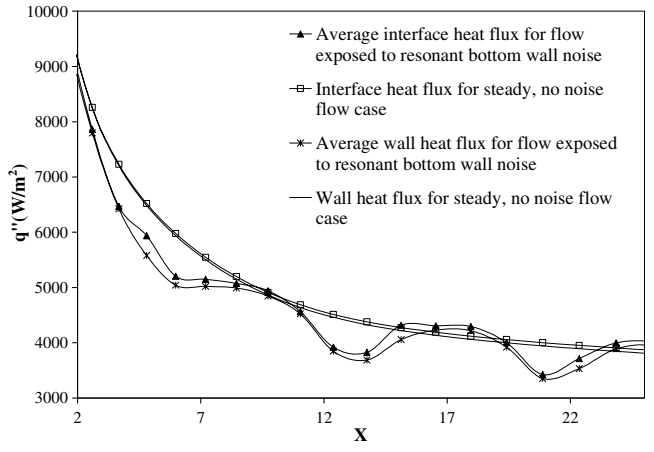

Fig. 16. For flow situations specified in Table 1 of the tube under zero gravity, the figure shows steady and time-averaged values of heat flux at the wall and at the interface. The noise is resonant with $v_1(x, 0,t) = \varepsilon \cdot \sin(2\pi x/\lambda) \cdot \sin(2\pi t/T)$, $\varepsilon = 0.35E{-}04$, $\lambda = 8$, and $T = T(x) = \lambda/\bar{u}_{steady}$.

12. Effects of waves on shear stress

12.1. Gravity driven cases

12.1.1. In-tube/channel geometries

For resonant noise, short-length, vertical in-tube cases; in Fig. 17, it is found that non-dimensional interfacial and wall shear (see definition of τ in [2]) show strong wave effects—with a clear wave induced enhancement in interfacial shear occurring only at large x.

12.2. Shear driven cases

12.2.1. In-tube/channel geometries

The in-tube cases, being similar to what has been discussed in [2] for the horizontal channel geometry, are not discussed here for brevity.

13. Summary of results

The computational and experimental results and associated flow regimes for constrained (i.e. prescribed or fixed) steady exit conditions are best summarized by Fig. 3. These flow regimes can be kept annular or annular-wavy over long distances.

For the commonly occurring unconstrained (or unspecified) exit-condition cases, there are various steady/quasi-steady and other flow regimes. These regimes for gravity and shear driven flows are respectively summarized by Fig. 4a, 4b and their captions. Clearly the relative lengths of the various flow regimes in Fig. 4a or Fig. 4b are functions of all the flow conditions (with inlet speed,

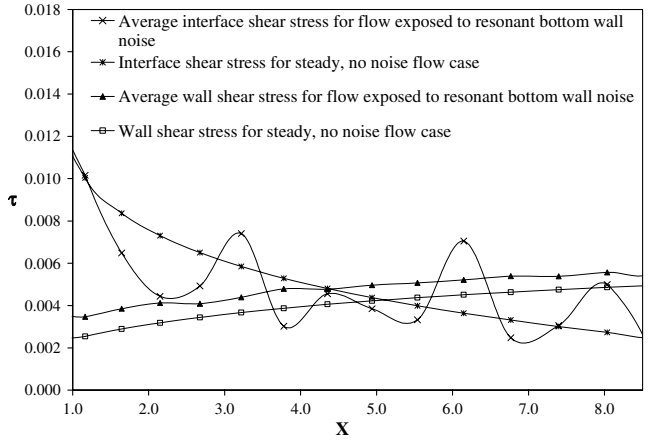

Fig. 17. For flow situations specified in Table 1 of the tube and vertical configuration, the figure shows steady and time-averaged values of shear stress at the wall and at the interface. The noise is resonant with $v_1(x, 0, t) = \varepsilon \cdot \sin(2\pi x/\lambda) \cdot \sin(2\pi t/T)$, $\varepsilon = 0.51E{-}04$, $\lambda = 2.6$, and $T = T(x) = \lambda/\bar{u}_{steady}$.

temperature difference ΔT, and exit location x_e in particular) that determine the flow.

14. Conclusions

By improving the accuracy of the interface tracking approach for the transient wavy flows, this paper extends/improves the results reported in [1,2] to longer duct lengths. By doing so, the paper discovers the hitherto unreported results that pertain to the loss of stability of the condensate flow at the larger downstream distances (e.g. $Re_\delta|_{cr} \approx 20$–$25$ for the gravity driven flows and $Re_\delta|_{cr} \approx 7$–$12$ for shear driven flows).

The following results reported in [1,2] were re-established and re-confirmed for the important in-tube condensing flow cases:

- For unconstrained exit conditions associated with nearly incompressible vapor flows, an unsteady noise-free simulation method for identifying the *natural* exit condition (exit pressure or exit quality) and its corresponding solution are shown to be possible for normal gravity and zero gravity cases over a length of a duct over which the flow regime is *parabolic*.
- The noise-sensitivity and resonance effects make the wave-free steady solutions quasi-steady and this is demonstrated by the inclusion of the effects of ubiquitous minuscule condensing surface vibrations that are always present.
- Heat transfer enhancements due to waves on the interface occur more readily in the presence of gravity driven condensate flows and this has been shown again for the in-tube cases.

Some other new results for the channel flow cases and zero gravity cases are presented here and they improve our understanding of shear driven cases. These results are:

- If there is inadequate shear available to drive the condensate, there may not exist a steady "natural" exit condition and associated quasi-steady solution. Alternatively, a natural steady solution may exist only over the high shear entrance zone. This has been established by demonstrating a downstream zone of convective instability (termed "loss of parabolicity") for certain shear driven channel and in-tube flows' steady solutions under unprescribed exit conditions.
- Effects of surface-tension were shown to be insignificant for all terrestrial environments (horizontal to vertical). Surface-tension was found to have an important stabilizing effect—particularly for zero gravity—where steady flows, if they exist, are often weakly stable.
- Sensitivity to small changes in the exit condition (particularly self-induced changes for unconstrained exits) are typically found for most shear driven flows as the flow regime they operate in are, quite commonly, *weakly parabolic* to *elliptic*.

Acknowledgement

This work was supported by the NSF grant CTS-0086988 and NASA grant NNC04GB52G.

Appendix

The differential forms of mass, momentum (x and y components, where $y \equiv 1 - r$), and energy equations in terms of non-dimensional variables for flows in the interior of either of the phases ($I = 1$ or 2) for the in-tube flows are given below:

$$\begin{aligned}
&\frac{\partial u_I}{\partial x} + \frac{1}{r}\frac{\partial}{\partial r}(r v_I) = 0,\\
&\frac{\partial u_I}{\partial t} + u_I\frac{\partial u_I}{\partial x} + v_I\frac{\partial u_I}{\partial r}\\
&\quad = \frac{1}{Re_I}\left[2\frac{\partial^2 u_I}{\partial x^2} + \frac{\partial^2 u_I}{\partial r^2} + \frac{\partial^2 v_I}{\partial x^2} - \frac{1}{r}\left(\frac{\partial u_I}{\partial r} + \frac{\partial v_I}{\partial x}\right)\right]\\
&\qquad - \frac{\partial \pi_I}{\partial x} + Fr_x^{-1},\\
&\frac{\partial v_I}{\partial t} + u_I\frac{\partial v_I}{\partial x} + v\frac{\partial v_I}{\partial r}\\
&\quad = \frac{1}{Re_I}\left[\frac{\partial}{\partial x}\left(\frac{\partial u_I}{\partial r}\right) + \frac{\partial^2 v_I}{\partial x^2} + \frac{2}{r}\left(r\frac{\partial^2 v_I}{\partial r^2} - \frac{\partial v_I}{\partial r} - \frac{v_I}{r}\right)\right]\\
&\qquad - \frac{\partial \pi_I}{\partial r} + Fr_r^{-1},\\
&\frac{\partial \theta_I}{\partial t} + u_I\frac{\partial \theta_I}{\partial x} + v_I\frac{\partial \theta_I}{\partial r} \approx \frac{1}{Re_I Pr_I}\left(\frac{\partial^2 \theta_I}{\partial x^2} + \frac{1}{r^2}\frac{\partial^2 \theta_I}{\partial r^2} - \frac{1}{r}\frac{\partial \theta_I}{\partial r}\right),
\end{aligned} \tag{A.1}$$

where $Re_I \equiv \rho_I U R/\mu_I$, $Pr_I \equiv \mu_I C_{p_I}/k_I$, $Fr_x^{-1} \equiv g_x R/U^2$ and $Fr_r^{-1} \equiv g_r R/U^2$.

The term [t] on the right side of Eq. (4) is given by

$$\begin{aligned}
[t] = &\left\{\frac{\mu_2}{\mu_1}\frac{\partial v_2}{\partial x}\Big|^i - \frac{\partial v_1}{\partial x}\Big|^i\right\} + \frac{2\delta_x}{[1-\delta_x^2]}\left\{\frac{\partial u_1}{\partial x}\Big|^i - \frac{\partial v_1}{\partial r}\Big|^i\right\}\\
&- \frac{2\delta_x}{[1-\delta_x^2]}\frac{\mu_2}{\mu_1}\left\{\frac{\partial u_2}{\partial x}\Big|^i - \frac{\partial v_2}{\partial r}\Big|^i\right\} + \frac{c_2 d_1 \rho_2 U}{\mu_1(\delta_x^2 - 1)}\sqrt{1+\delta_x^2}\frac{\partial \pi_2}{\partial x}\Big|^i,
\end{aligned} \tag{A.2}$$

where $c_2 \equiv -\,d\sigma/dT \approx 0.122$ N/m/K (for FC-72) and 0.1046 N/m/K (for R-113), and $d_1 \equiv dT/dp \approx 0.0003$ K/Pa (for FC-72) and 0.0003 K/Pa (for R-113).

References

[1] A. Narain, Q. Liang, G. Yu, X. Wang, Direct computational simulations for internal condensing flows and results on attainability/stability of steady solutions, their intrinsic waviness, and their noise-sensitivity, J. Appl. Mech. 71 (2004) 69–88.

[2] Q. Liang, X. Wang, A. Narain, Effect of gravity, shear and surface tension in internal condensing flows—results from direct computational simulations, ASME J. Heat Transfer 126 (5) (2004) 676–686.

[3] A. Narain, A. Siemionko, T.W. Ng, J.H. Kurita, N. Kim, K. Opella, P.O. Sweger, Internal condensing flows inside a vertical pipe—experimental/computational investigations of effects of constrained and natural exit conditions, in: Proceedings of the ASME

International Mechanical Engineering Congress and Exposition, November 5–11, 2005, Orlando, FL, USA. Paper no. IMECE2005–80441 on the CD-ROM with ISBN 0-7918-3769-6. Also submitted for publication in the ASME Journal of Heat Transfer (2006) and available at: <http://www.me.mtu.edu/~narain>.

[4] W. Nusselt, Die oberflächenkondesation des wasserdampfes, Z. Ver. Dt. Ing. 60 (27) (1916) 541–546.

[5] W.M. Rohsenow, Heat transfer and temperature distribution in laminar film condensation, Trans. ASME 78 (1956) 1645–1648.

[6] E.M. Sparrow, J.L. Gregg, A boundary layer treatment of laminar film condensation, ASME J. Heat Transfer 81 (1959) 13–18.

[7] J.C.Y. Koh, E.M. Sparrow, J.P. Hartnett, The tow-phase boundary layer in laminar film condensation, Int. J. Heat Mass Transfer 2 (1961) 69–82.

[8] V.K. Dhir, J.H. Lienhard, Laminar film condensation on plane and axisymmetric bodies in non-uniform gravity, J. Heat Transfer 93 (1971) 97–100.

[9] R.D. Cess, Laminar film condensation on a flat plate in the absence of a body force, Z. Angew. Math. Phys. 11 (1960) 426–433.

[10] J.C.Y. Koh, Film condensation in a forced-convection boundary-layer flow, Int. J. Heat Mass Transfer 5 (1962) 941–954.

[11] L. Phan, A. Narain, The classical Nusselt problem of film condensation—direct steady and unsteady computational simulations that yield results on stability and wave effects, in: Proceedings of the ASME International Mechanical Engineering Congress and Exposition, November 5–11, 2005, Orlando, FL, USA. Paper no. IMECE2005-80221 on the CD-ROM with ISBN 0-7918-3769-6. Also accepted for publication in ASME Journal of Applied Mechanics (2006) and available at: <http://www.me.mtu.edu/~narain>.

[12] G. Son, V.K. Dhir, Numerical simulation of film boiling near critical pressures with a level set method, J. Heat Transfer 120 (1998) 183–192.

[13] M. Sussman, P. Smereka, S. Osher, A level set approach for computing solutions to incompressible two-phase flow, J. Comput. Phys. 114 (1994) 146–159.

[14] C.W. Hirt, B.D. Nichols, Volume of fluid (VOF) method for the dynamics of free boundaries, J. Comput. Phys. 39 (1981) 201–255.

[15] A. Esmaeeli, G. Tryggvason, Computations of film boiling—Part i: Numerical method, Int. J. Heat Mass Transfer 47&25 (2004) 5451–5461.

[16] D. Juric, G. Tryggvason, Computations of boiling flows, Int. J. Multiphase Flow 24 (1998) 387–410.

[17] T.E. Tezduyar, Finite element methods for flow problems with moving boundaries and interfaces, Arch. Comput. Methods Engrg. 8 (2001) 83–130.

[18] M.A Cruchaga, D.J. Celentano, T.E. Tezduyar, Moving-interface computations with the edge-tracked interface locator technique (ETILT), Int. J. Numer. Methods Fluids 47 (2005) 451–469.

[19] M.B. Abbott, D.R. Basco, Computational Fluid Dynamics—An Introduction for Engineers, Longman, 1989, Chapter 3, pp. 86–88 and Chapter 5, pp. 151–155.

[20] A. Narain, G. Yu, Q. Liu, Interfacial shear models and their required asymptotic form for annular/stratified film condensation flows in inclined channels and vertical pipes, Int. J. Heat Mass Transfer 40 (15) (1997) 3559–3575.

[21] D.P Traviss, W.M. Rohsenow, A.B. Baron, Forced-convection condensation inside tubes: a heat transfer equation for condenser design, ASHRAE Trans. 79 (Part 1) (1973) 157–165.

[22] M.M. Shah, A general correlation for heat transfer during film condensation inside pipes, Int. J. Heat Mass Transfer 22 (1979) 547–556.

[23] G.F. Hewitt, G.L. Shires, Y.V. Polezhaev (Eds.), International Encyclopedia of Heat and Mass Transfer, CRC Press, Boca Raton and New York, 1997.

[24] V.P. Carey, Liquid–Vapor Phase-Change Phenomena, Series in Chemical and Mechanical Engineering, Hemisphere Publishing Corporation, 1992.

[25] J.W. Palen, R.S. Kistler, Y.Z Frank, What we still don't know about condensation in tubes, in: J. Taborek, J. Rose, I. Tanasawa, Condensation and Condenser Design, United Engineering Trustees, Inc. for Engineering Foundation and ASME, New York, 1993, pp. 19–53.

[26] J.M. Delhaye, Jump conditions and entropy sources in two-phase systems; local instant formulation, Int. J. Multiphase Flow 1 (1974) 395–409.

[27] X. Wang, Direct computational studies and code development for condensing flows inside tubes and channels—an investigation of stability and noise-sensitivity issues under different conditions of gravity and surface-tension, Ph.D. thesis, Michigan Technological University, Houghton, Michigan, 2006.

[28] ASHRAE Handbook, Fundamentals SI Edition, American Society of Heating, Refrigeration and Air-Conditioning Engineers, Inc., Atlanta, GA, 1985.